J. Fluid Mech. (2014), *vol.* 747, *pp.* 1–29.
doi:10.1017/jfm.2014.134

Optimal Taylor–Couette flow: radius ratio dependence

Rodolfo Ostilla-Mónico[1,†], Sander G. Huisman[1], Tim J. G. Jannink[1], Dennis P. M. Van Gils[1], Roberto Verzicco[1,2], Siegfried Grossmann[3], Chao Sun[1] and Detlef Lohse[1]

[1]Physics of Fluids, Mesa+ Institute, University of Twente, PO Box 217, 7500 AE Enschede, The Netherlands

[2]Dipartimento di Ingegneria Meccanica, University of Rome 'Tor Vergata', via del Politecnico 1, 00133 Roma, Italy

[3]Department of Physics, University of Marburg, Renthof 6, 35032 Marburg, Germany

(Received 23 April 2013; revised 22 January 2014; accepted 5 March 2014; first published online 10 April 2014)

Taylor–Couette flow with independently rotating inner (i) and outer (o) cylinders is explored numerically and experimentally to determine the effects of the radius ratio η on the system response. Numerical simulations reach Reynolds numbers of up to $Re_i = 9.5 \times 10^3$ and $Re_o = 5 \times 10^3$, corresponding to Taylor numbers of up to $Ta = 10^8$ for four different radius ratios $\eta = r_i/r_o$ between 0.5 and 0.909. The experiments, performed in the Twente Turbulent Taylor–Couette (T^3C) set-up, reach Reynolds numbers of up to $Re_i = 2 \times 10^6$ and $Re_o = 1.5 \times 10^6$, corresponding to $Ta = 5 \times 10^{12}$ for $\eta = 0.714$–0.909. Effective scaling laws for the torque $J^\omega(Ta)$ are found, which for sufficiently large driving Ta are independent of the radius ratio η. As previously reported for $\eta = 0.714$, optimum transport at a non-zero Rossby number $Ro = r_i|\omega_i - \omega_o|/[2(r_o - r_i)\omega_o]$ is found in both experiments and numerics. Here Ro_{opt} is found to depend on the radius ratio and the driving of the system. At a driving in the range between $Ta \sim 3 \times 10^8$ and $Ta \sim 10^{10}$, Ro_{opt} saturates to an asymptotic η-dependent value. Theoretical predictions for the asymptotic value of Ro_{opt} are compared to the experimental results, and found to differ notably. Furthermore, the local angular velocity profiles from experiments and numerics are compared, and a link between a flat bulk profile and optimum transport for all radius ratios is reported.

Key words: convection, Taylor–Couette flow

1. Introduction

Taylor–Couette (TC) flow consists of the flow between two coaxial cylinders that are independently rotating. A schematic drawing of the system can be seen in figure 1. The rotation difference between the cylinder shears the flow, thus driving the system. This rotation difference has been traditionally expressed by two Reynolds numbers, the inner cylinder $Re_i = r_i\omega_i d/\nu$ and the outer cylinder $Re_o = r_o\omega_o d/\nu$ Reynolds numbers, where r_i and r_o are the radii of the inner and outer cylinder, respectively, ω_i and ω_o

†Email address for correspondence: R.Ostillamonico@utwente.nl

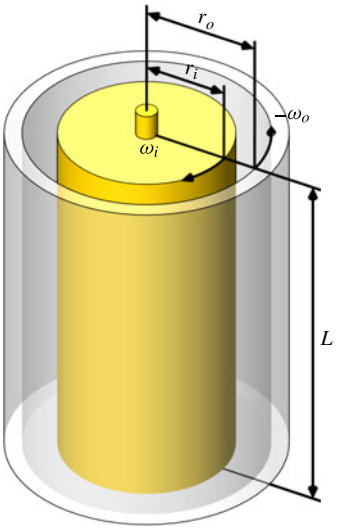

FIGURE 1. (Colour online) Schematic of the Taylor–Couette system. The system consists of two coaxial cylinders, which have an inner cylinder radius of r_i and an outer cylinder radius of r_o. Both cylinders are of length L. The inner cylinder rotates with an angular velocity ω_i and the outer cylinder rotates with an angular velocity of ω_o.

the inner and outer cylinder angular velocity, $d = r_o - r_i$ the gap width, and ν the kinematic viscosity. The geometry of TC flow is characterized by two non-dimensional parameters, namely the radius ratio $\eta = r_i/r_o$ and the aspect ratio $\Gamma = L/d$.

Instead of taking Re_i and Re_o, the driving in TC flow can alternatively be characterized by the Taylor number Ta and the rotation rate, also called the Rossby number Ro. The Taylor number can be seen as the non-dimensional forcing (the differential rotation) of the system defined as $Ta = \sigma(r_o - r_i)^2(r_o + r_i)^2(\omega_o - \omega_i)^2/(4\nu^2)$, or

$$Ta = (r_a^6 d^2/r_o^2 r_i^2 \nu^2)(\omega_o - \omega_i)^2. \tag{1.1}$$

Here $\sigma = r_a^4/r_g^4$ with $r_a = (r_o + r_i)/2$ the arithmetic and $r_g = \sqrt{r_o r_i}$ the geometric mean radii. The Rossby number is defined as

$$Ro = \frac{|\omega_i - \omega_o| r_i}{2\omega_o d}, \tag{1.2}$$

and can be seen as a measure of the rotation of the system as a whole. Here $Ro < 0$ corresponds to counter-rotating cylinders, and $Ro > 0$ to co-rotating cylinders.

TC flow is among the most investigated systems in fluid mechanics, mainly owing to its simplicity as an experimental model for shear flows. TC flow is in addition a closed system, so global balances that relate the angular velocity transport to the energy dissipation can be obtained. Specifically, in Eckhardt, Grossmann & Lohse (2007, hereafter referred to as EGL07), an exact relationship between the global parameters and the volume-averaged energy dissipation rate was derived. This relationship has an analogous form to the one that can be obtained for Rayleigh–Bénard (RB) flow, i.e. a flow in which heat is transported from a hot bottom plate to a cold top plate.

TC and RB flows have been extensively used to explore new concepts in fluid mechanics. Instabilities (Busse 1967; Chandrasekhar 1981; Drazin & Reid 1981; Pfister & Rehberg 1981; Swinney & Gollub 1981; Pfister *et al.* 1988), nonlinear dynamics and chaos (Lorenz 1963; Ahlers 1974; Behringer 1985; Dominguez-Lerma, Cannell & Ahlers 1986; Strogatz 1994), pattern formation (Andereck, Liu & Swinney 1986; Cross & Hohenberg 1993; Bodenschatz, Pesch & Ahlers 2000) and turbulence (Lathrop, Fineberg & Swinney 1992*b*; Siggia 1994; Grossmann & Lohse 2000; Kadanoff 2001; Ahlers, Grossmann & Lohse 2009; Lohse & Xia 2010) have been studied in both TC and RB flows, and both numerically and experimentally. The main reasons behind the popularity of these systems are, in addition to the fact that they are closed systems, as mentioned previously, their simplicity due to the high amount of symmetries present. It is also worth noting that plane Couette flow is the limiting case of TC flow when the radius ratio $\eta = 1$.

Experimental investigations of TC flow have a long history, dating back to the initial work at the end of the 1800s by Couette (1890) in France, who concentrated on outer cylinder rotation and developed the viscometer, and Mallock (1896) in the UK, who also rotated the inner cylinder and found indications of turbulence. Later work by Wendt (1933) and Taylor (1936), greatly expanded on the system, the former measuring torques and velocities for several radius and rotation ratios in the turbulent case, and the latter being the first to mathematically describe the cells that form if the flow is linearly unstable. The subject can be traced back even further to Stokes, and even Newton. For a broader historical context, we refer the reader to Donnelly (1991).

Experimental work continued over the years (Smith & Townsend 1982; Andereck *et al.* 1986; Tong *et al.* 1990; Lathrop, Fineberg & Swinney 1992*a*; Lathrop *et al.* 1992*b*; Lewis & Swinney 1999; van Gils *et al.* 2011*a*,*b*; Paoletti & Lathrop 2011; Huisman *et al.* 2012*b*) at low and high Ta and for different ratios of the rotation frequencies $a = -\omega_o/\omega_i$; thus a is positive for counter-rotation and negative for co-rotation. Here $-a \equiv \mu$, another measure used for the ratio of rotation frequencies. This work has been complemented by numerical simulations, not only in the regime of pure inner cylinder rotation (Fasel & Booz 1984; Coughlin & Marcus 1996; Dong 2007, 2008; Pirro & Quadrio 2008), but also for eigenvalue study (Gebhardt & Grossmann 1993) and counter-rotation at fixed a (Dong 2008). Recently (Brauckmann & Eckhardt 2013*a*; Ostilla *et al.* 2013), simulations have also explored the effect of the outer cylinder rotation on the system at large Reynolds numbers.

The recent experiments (van Gils *et al.* 2011*a*,*b*; Paoletti & Lathrop 2011; Merbold, Brauckmann & Egbers 2013) and simulations (Brauckmann & Eckhardt 2013*a*; Ostilla *et al.* 2013) have shown that at fixed Ta an optimal angular momentum transport is obtained at *non-zero* a_{opt}, and that the location of this maximum a_{opt} varies with Ta. However, both experiments and simulations have been restricted to two radius ratios, namely $\eta = 0.5$ and $\eta = 0.714$. The same radius ratios were also used for studies carried out on scaling laws of the torque and the 'wind' of turbulence at highly turbulent Taylor numbers (Lewis & Swinney 1999; van Gils *et al.* 2011*b*; Paoletti & Lathrop 2011; Huisman *et al.* 2012*b*; Merbold *et al.* 2013). Up to now, it is not clear how the radius ratio affects the scaling laws of the system response or the recently found phenomena of optimal transport as a function of Ta.

Two suggestions were made to account for the radius ratio dependence of optimal transport. Van Gils *et al.* (2011*b*) wondered whether the optimal transport in general lies in or at least close to the Voronoi boundary (meaning a line of equal distance) of the Esser–Grossmann stability lines (Esser & Grossmann 1996) in the (Re_o, Re_i) phase

space as it does for $\eta = 0.714$. However, this bisector value does not give the correct optimal transport for $\eta = 0.5$ (Brauckmann & Eckhardt 2013*b*; Merbold *et al.* 2013). Therefore, Brauckmann & Eckhardt (2013*a*) proposed a dynamic extension of the Esser–Grossmann instability theory. This model correctly gives the observed optimal transport (within experimental error bars) between $\eta = 0.5$ and $\eta = 0.714$ for three experimental datasets (Wendt 1933; van Gils *et al.* 2011*b*; Paoletti & Lathrop 2011) and one numerical dataset (Brauckmann & Eckhardt 2013*b*), but it is not clear how it performs outside the η range [0.5, 0.714].

In this paper, we study the following questions. How does the radius ratio η affect the flow? How are the scaling laws of the angular momentum transport affected? What is the role of the geometric parameter called the pseudo-Prandtl number σ introduced in EGL07? Can the effect of the radius ratio be interpreted as a kind of non-Oberbeck–Boussinesq effect, analogous to this effect in Rayleigh–Bénard flow? Finally, are the predictions and insights of van Gils *et al.* (2011*b*), Brauckmann & Eckhardt (2013*b*) and Ostilla *et al.* (2013) on the optimal transport also valid for other values of η?

In order to answer these questions, both direct numerical simulations (DNS) and experiments have been undertaken. Numerical simulations, with periodic axial boundary conditions, have been performed using the finite-difference code previously used in Ostilla *et al.* (2013). In these simulations, three more values of η have been investigated: one in which the gap is larger ($\eta = 0.5$), and two in which the gap is smaller ($\eta = 0.833$ and 0.909). With the previous simulations from Ostilla *et al.* (2013) at $\eta = 0.714$, a total of four radius ratios has been analysed.

In both experiments and numerics, only one aspect ratio Γ has been studied for every radius ratio. Since the work of Benjamin (1978) it has been known that multiple flow states with a different amount of vortex pairs can coexist in TC flow for the same non-dimensional flow parameters. However, with increased driving, the bifurcations become less important and many branches do not survive. Indeed Lewis & Swinney (1999) found that for pure inner cylinder rotation only one branch with eight vortices (for $\Gamma = 11.4$ and $\eta = 0.714$) remains when Re_i is increased above 2×10^4. As the Reynolds numbers reached in the experiments greatly exceed this value, we do not expect to see the effect of multiple states in the current experimental results.

For the numerical simulations, axially periodic boundary conditions have been taken. Brauckmann & Eckhardt (2013*a*) already studied the effect of the axial periodicity length on the system, and found that, for a fixed vortical wavelength, the number of vortices does not affect the overall flow behaviour. It was also found that, in analogy to experiments, the effect of vortical wavelength, and hence of multiple states, becomes smaller with increased driving. However, changes between states can still be seen for small drivings.

Figure 2 shows the (Ta, $1/Ro$) parameter space explored in the simulations for the four selected values of the radius ratio η. A higher density of points has been used in places where the global response (Nu_ω, Re_w) of the flow shows more variation with the control parameters Ta and $1/Ro$. A fixed aspect ratio of $\Gamma = 2\pi$ has been taken for all simulations, and axially periodic boundary conditions have been used. These simulations have the same upper bounds of Ta (or Re_i) as those of Ostilla *et al.* (2013).

In addition to these simulations, experiments have been performed with the Twente Turbulent Taylor–Couette (T^3C) facility, with which we achieve larger Ta numbers. Details of the set-up are given in van Gils *et al.* (2011*a*). Once again, four values of η have been investigated, but, owing to experimental constraints, we have been limited to investigate only smaller gap widths, i.e. values $\eta \geqslant 0.716$, namely $\eta = 0.716$, 0.769,

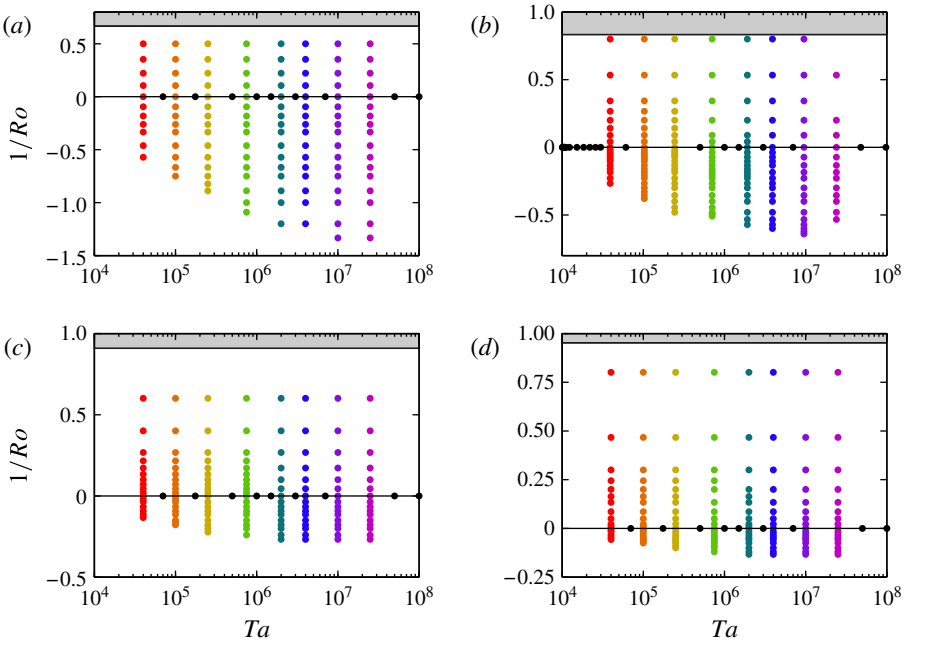

FIGURE 2. (Colour online) The control parameter phase space that was numerically explored in this paper in the $(Ta, 1/Ro)$ representation: (*a*) $\eta = 0.5$, (*b*) $\eta = 0.714$, (*c*) $\eta = 0.833$ and (*d*) $\eta = 0.909$. Here $\Gamma = 2\pi$ was fixed, and axial periodicity was employed. The grey shaded area signals boundary conditions for which the angular momentum $L = r^2\omega$ of the outer cylinder (L_o) is larger than the angular momentum of the inner cylinder (L_i). This causes the flow to have an overall transport of angular momentum towards the inner cylinder. In this region, the Rayleigh stability criterion applies, which states that if $\mathrm{d}L^2/\mathrm{d}r > 0$ then the flow is linearly stable to axisymmetric perturbations.

0.833 and 0.909. (In the experimental setup, $\eta = 0.716$, while in the simulations $\eta = 0.714$ is used. These two are directly compared to each other in the manuscript. When referring to either numerical data, or numerical and experimental data in combination, $\eta = 0.714$ is used, while when referring to exclusively experimental data, $\eta = 0.716$ is used.) The experimentally explored parameter space is shown in figure 3.

The structure of the paper is as follows. In §§ 2 and 3, we start by describing the numerical code and the experimental set-up, respectively. In § 4, the global response of the system, quantified by the non-dimensionalized angular velocity current Nu_ω, is analysed. To understand the global response, we analyse the local data that can be obtained from the DNS in § 5. Angular velocity profiles in the bulk and in the boundary layers are analysed and related to the global angular velocity optimal transport. We finish in § 6 with a discussion of the results and an outlook for further investigations.

2. Numerical method

In this section, the numerical method used is explained in some detail. The rotating frame in which the Navier–Stokes equations are solved and the employed

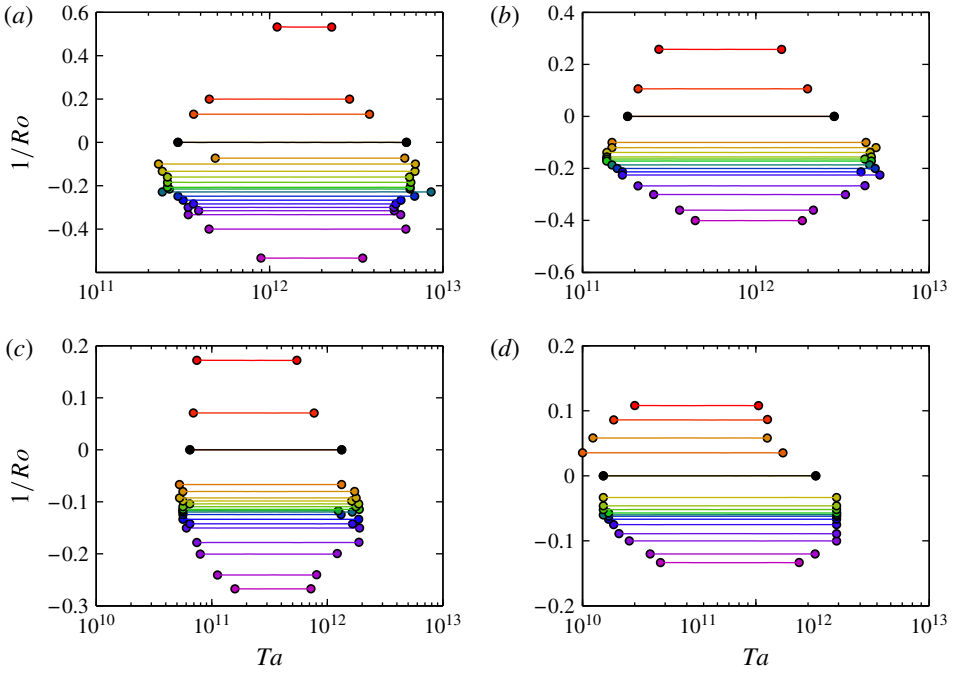

FIGURE 3. (Colour online) The control parameter phase space that was explored in the experiments in the (Ta, Ro^{-1}) representation: (a) $\eta = 0.716$, (b) $\eta = 0.769$, (c) $\eta = 0.833$ and (d) $\eta = 0.909$.

non-dimensionalizations are introduced is described in § 2.1. This is followed in § 2.2 by detailing the spatial resolution checks that have been performed.

2.1. *Code description*

The employed code is a finite-difference code, which solves the Navier–Stokes equations in cylindrical coordinates. A second-order spatial discretization is used, and the equations are advanced in time by a fractional time integration method. This code is based on the so-called Verzicco code, whose numerical algorithms are detailed in Verzicco & Orlandi (1996). A combination of MPI and OpenMP directives are used to achieve large-scale parallelization. This code has been extensively used for Rayleigh–Bénard flow; for recent simulations see Stevens, Verzicco & Lohse (2010) and Stevens, Lohse & Verzicco (2011). In the context of TC flow, Ostilla *et al.* (2013) have already validated the code for $\eta = 0.714$.

The flow was simulated in a rotating frame, which was chosen to rotate with $\Omega = \omega_o \boldsymbol{e}_z$. This was done in order to simplify the boundary conditions. In that frame, the outer cylinder is stationary for any value of a, while the inner cylinder has an azimuthal velocity of $u_\theta(r = r_i) = r_i(\omega_i^\ell - \omega_o^\ell)$, where the superscript ℓ denotes variables in the laboratory frame, while no superscript denotes variables in the rotating frame. We then choose the inner cylinder rotation rate in the rotating frame as the characteristic velocity of the system $U \equiv |u_\theta(r_i)| = r_i|\omega_i - \omega_o|$ and the characteristic length scale d to non-dimensionalize the equations and boundary conditions.

Using this non-dimensionalization, the inner cylinder velocity boundary condition simplifies to $\hat{u}_\theta(r = r_i) = \mathrm{sgn}(\omega_i - \omega_o)$. In this paper, $\omega_i - \omega_o$ is always positive. Thus,

in this rotating frame the flow geometry is simplified to a pure inner cylinder rotation with the boundary condition $\hat{u}_\theta(r_i) = 1$. The outer cylinder's effect on the flow is felt as a Coriolis force in this rotating frame of reference. The Navier–Stokes equations then read

$$\frac{\partial \hat{\boldsymbol{u}}}{\partial \hat{t}} + \hat{\boldsymbol{u}} \cdot \hat{\boldsymbol{\nabla}} \hat{\boldsymbol{u}} = -\hat{\boldsymbol{\nabla}} \hat{p} + \left(\frac{f(\eta)}{Ta} \right)^{1/2} \hat{\nabla}^2 \hat{\boldsymbol{u}} + Ro^{-1} \boldsymbol{e}_z \times \hat{\boldsymbol{u}}, \tag{2.1}$$

where Ro was defined previously in (1.2), and $f(\eta)$ is

$$f(\eta) = \frac{(1+\eta)^3}{8\eta^2}. \tag{2.2}$$

It is useful to continue the non-dimensionalization by defining the normalized radius $\tilde{r} = (r - r_i)/d$ and the normalized height $\tilde{z} = z/d$. We define the time- and azimuthally averaged velocity field as

$$\hat{\bar{\boldsymbol{u}}}(r, z) = \langle \hat{\boldsymbol{u}}(\theta, r, z, t) \rangle_{\theta,t}, \tag{2.3}$$

where $\langle \phi(x_1, x_2, \ldots, x_n) \rangle_{x_i}$ indicates averaging of the field ϕ with respect to x_i.

To quantify the torque in the system, we first note that the angular velocity current

$$J^\omega = r^3 (\langle u_r^\ell \omega^\ell \rangle_{\theta,z,t} - \nu \partial_r \langle \omega^\ell \rangle_{\theta,z,t}) \tag{2.4}$$

is conserved, i.e. independent of the radius r (EGL07). Here J^ω represents the current of angular velocity from the inner cylinder to the outer cylinder (or vice versa). The first term is the convective contribution to the transport, while the second term is the diffusive contribution.

In the state with the lowest driving, and ignoring end-plate effects, a laminar, time-independent velocity field that is purely azimuthal, $u_\theta^\ell(r) = Ar + B/r$, with $u_r = u_z = 0$, is induced by the rotating cylinders. This laminar flow produces an angular velocity current J_0^ω, which can be used to non-dimensionalize the angular velocity current,

$$Nu_\omega = \frac{J^\omega}{J_0^\omega}; \tag{2.5}$$

Nu_ω can be seen as an angular velocity 'Nusselt' number.

When J^ω, and therefore Nu_ω, are calculated numerically, the values will depend on the radial position, owing to finite time averaging. We can define Δ_J to quantify this radial dependence as

$$\Delta_J = \frac{\max(J^\omega(r)) - \min(J^\omega(r))}{\langle J^\omega(r) \rangle_r} = \frac{\max(Nu_\omega(r)) - \min(Nu_\omega(r))}{\langle Nu_\omega(r) \rangle_r}, \tag{2.6}$$

which analytically equals zero but will deviate when calculated numerically.

The convective dissipation per unit mass can be calculated from its definition as a volume average of the local dissipation rate for an incompressible fluid,

$$\epsilon_u = \epsilon_u^\ell = \frac{\nu}{2} \left\langle (\partial_i^\ell u_j + \partial_j^\ell u_i)^2 \right\rangle_{V,t}, \tag{2.7}$$

or a global balance can be used. The exact relationship (EGL07)

$$\epsilon_u^\ell - \epsilon_{u,0}^\ell = \frac{\nu^3}{d^4} \sigma^{-2} Ta (Nu_\omega - 1), \tag{2.8}$$

where $\epsilon_{u,0}$ is the volume-averaged dissipation rate in the purely azimuthal laminar flow, links the volume-averaged dissipation to the global driving Ta and response Nu_ω.

This link can be and has been used for code validation and for checking spatial resolution adequateness. The volume-averaged dissipation can be calculated from both

(2.7) and (2.8) and later checked for sufficient agreement. We define the quantity Δ_ϵ as the relative difference between the two ways of numerically calculating the dissipation, namely either via Nu_ω with (2.8) or directly from the velocity gradients, equation (2.7),

$$\Delta_\epsilon = \frac{\nu^3 d^{-4}\sigma^{-2} Ta(Nu_\omega - 1) + \epsilon_{u,0} - \frac{1}{2}\nu \left\langle (\partial_i u_j^\ell + \partial_j^\ell u_i)^2 \right\rangle_{V,t}}{\frac{1}{2}\nu \left\langle (\partial_i^\ell u_j + \partial_j^\ell u_i)^2 \right\rangle_{V,t}}. \tag{2.9}$$

The quantity Δ_ϵ is equal to zero analytically, but will deviate when calculated numerically. The deviation of Δ_J and Δ_ϵ from zero is an indication of the adequateness of the resolution.

We would like to emphasize that the requirement for $\Delta_J < 0.01$ is much stricter than torque balance, which can simply be expressed as $Nu_\omega(r_i) = Nu_\omega(r_o)$. As analysed in Ostilla *et al.* (2013), a value of less than 1 % for Δ_J and $\sim$1 % for Δ_ϵ is linked to grid adequateness at the Taylor number simulated. To ensure convergence in time, the time averages of the Nusselt number and the energy dissipation calculated locally (equation (2.7)) were also checked to converge in time within 1 %.

2.2. *Resolution checks*

Spatial resolution checks were performed in two ways. First, as mentioned previously, the values of Δ_J and Δ_ϵ were checked. As an additional check, simulations at selected values of Ta were performed at a higher resolution. As the explored parameter space is large, these checks were performed only for the highest value of Ta simulated for the grid size. A lower driving of the flow for the same grid size is expected to have a smaller error due to spatial discretization, as spatial discretization errors increase with increased Re, and thus increased Ta.

Concerning the temporal resolution, there are numerical and physical constraints. The former requires a time step small enough to keep the integration scheme stable, and this is achieved by using an adaptive time step based on a Courant–Friedrichs–Lewy (CFL) criterion. The third-order Runge–Kutta time-marching algorithm allows for a CFL of up to $\sqrt{3}$, but this can be reduced due to the implicit factorization of the viscous terms. For safety, the maximum CFL has been taken as 1.4. From the physical point of view, the time step size must also be small enough to properly describe the fast dynamics of the smallest flow scale, which is the Kolmogorov scale. Although the time step size should be determined by the most restrictive among the two criteria above, our experience suggests that, as long as the CFL number criterion is satisfied, which guarantees numerical stability, the results become insensitive to the time step size and all the flow scales are adequately described temporally. Direct confirmation of this statement can be found in Ostilla *et al.* (2013).

The results for $\eta = 0.5$, 0.833 and 0.909 are presented in table 1. Uniform discretization was used in the azimuthal and axial directions. In the radial direction, points were clustered near the walls by using hyperbolic tangent-type clustering, or a clipped Chebyshev-type clustering for higher values of Ta. A table including the results for the spatial resolution tests at $\eta = 0.714$ can be found in Ostilla *et al.* (2013).

3. Experimental set-up

The T^{3}C apparatus has been built to obtain high Ta numbers. It has been described in detail in van Gils *et al.* (2011*a*, 2012). The inner cylinder with outside radius $r_i =$ 0.200 m consists of three sections. The total height of those axially stacked sections is

η	Ta	$N_\theta \times N_r \times N_z$	Nu_ω	$100\Delta_J$	$100\Delta_\epsilon$	Case
0.5	2.5×10^5	$100 \times 100 \times 100$	2.03372	0.30	1.11	R
0.5	2.5×10^5	$150 \times 150 \times 150$	2.03648	0.76	0.89	E
0.5	7.5×10^5	$150 \times 150 \times 150$	2.56183	0.47	0.92	R
0.5	7.5×10^5	$256 \times 256 \times 256$	2.55673	0.74	0.31	E
0.5	1×10^7	$300 \times 300 \times 300$	4.23128	0.33	1.07	R
0.5	1×10^7	$400 \times 400 \times 400$	4.22574	0.97	1.06	E
0.5	2.5×10^7	$350 \times 350 \times 350$	5.07899	0.85	1.12	R
0.5	2.5×10^7	$512 \times 512 \times 512$	5.08193	0.87	1.98	E
0.5	5×10^7	$768 \times 512 \times 1536$	6.08284	0.45	1.56	R
0.5	1×10^8	$768 \times 512 \times 1536$	7.48561	1.46	0.88	R
0.833	2.5×10^5	$180 \times 120 \times 120$	2.72293	0.21	0.76	R
0.833	2.5×10^5	$300 \times 180 \times 180$	2.72452	0.29	0.29	E
0.833	1×10^7	$384 \times 264 \times 264$	7.07487	0.29	0.61	R
0.833	1×10^7	$512 \times 384 \times 384$	7.17245	0.13	1.16	E
0.833	2.5×10^7	$512 \times 384 \times 384$	8.62497	0.71	1.05	R
0.833	2.5×10^7	$768 \times 576 \times 576$	8.51678	0.90	1.26	E
0.833	5×10^7	$512 \times 384 \times 384$	9.68437	0.26	2.92	R
0.833	1×10^8	$768 \times 576 \times 576$	11.4536	0.89	2.29	R
0.909	2.5×10^5	$180 \times 120 \times 120$	2.31902	0.16	0.91	R
0.909	2.5×10^5	$300 \times 200 \times 200$	2.30810	0.07	0.17	E
0.909	2×10^6	$256 \times 180 \times 180$	3.76826	0.55	0.49	R
0.909	2×10^6	$384 \times 256 \times 256$	3.77532	0.39	0.21	E
0.909	2.5×10^7	$384 \times 256 \times 256$	7.83190	0.43	3.15	R
0.909	2.5×10^7	$450 \times 320 \times 320$	7.86819	0.81	2.07	E
0.909	5×10^7	$2305 \times 400 \times 1536$	9.74268	0.46	1.02	R
0.909	1×10^8	$2305 \times 400 \times 1536$	11.3373	0.57	1.06	R

TABLE 1. Resolution tests for $\Gamma = 2\pi$ and $\eta = 0.5$, 0.833 and 0.909. The columns display the radius ratio, the Taylor number, the resolution employed, the calculated Nu_ω, the relative discrepancies Δ_J and Δ_ϵ, and finally the 'case': resolved (R) and error (E) reference. Here Δ_ϵ is positive, and exceeds the 1 % threshold reported in Ostilla *et al.* (2013) for some cases at the largest η, but even so resolution appears to be sufficient as variations of Nu_ω are small.

$L = 0.927$ m. We measure the torque only on the middle section of the inner cylinder, which has a height of $L_{mid} = 0.536$ m, to reduce the effect of the torque losses at the end plates in our measurements. This approach has already been validated in van Gils *et al.* (2012). The transparent outer cylinder is made of acrylic and has an inside radius of $r_o = 0.2794$ m. We vary the radius ratio by reducing the diameter of the outer cylinder by adding a 'filler' that is fixed to the outer cylinder and sits between the inner and the outer cylinder, effectively reducing r_o while keeping r_i fixed. We have three fillers giving us four possible outer radii: $r_o = 0.2794$ m (without any filler), 0.26 m, 0.24 m and 0.22 m, giving experimental access to $\eta = 0.716$, 0.769, 0.833 and 0.909, respectively. Note that by reducing the outer radius, we not only change η, but also change $\Gamma = L/(r_o - r_i)$ from $\Gamma(\eta = 0.716) = 11.68$ to $\Gamma(\eta = 0.909) = 46.35$.

For high Ta the heating up of the system becomes apparent and it has to be actively cooled in order to keep the temperature constant. We cool the working fluid (water) from the top and bottom end plates and maintain a constant temperature

within ± 0.5 K through both the spatial extent and the time run of the experiment. The set-up has been constructed in such a way that we can rotate the two cylinders independently while keeping the set-up cooled.

As we said before, we measure the torque on the middle inner cylinder. We do this by measuring the torque that is transferred from the axis to the cylinder by using a load cell that is inside the aforementioned cylinder. Torque measurements are performed using a fixed procedure. The inner cylinder is spun up to its maximum rotational frequency of 20 Hz and kept there for several minutes. Then the system is brought to rest. The cylinders are then brought to their initial rotational velocities (with the chosen $1/Ro$), corresponding to a velocity for which the torque is accurate enough; generally of order 2–3 Hz. We then slowly increase both velocities over 3 to 6 h to their final velocities while maintaining $1/Ro$ fixed during the entire experiment. During this velocity ramp, we continuously acquire the torque of this quasi-stationary state. The calibration of the system is done in a similar way; first we apply the maximum load on the system, going back to zero load, and then gradually adding weight while recording the torque. These procedures ensure that hysteresis effects are kept to a minimum, and that the system is always brought to the same state before measuring. More details about the set-up can be found in van Gils *et al.* (2011*a*).

Local velocity measurements are done by laser Doppler anemometry (LDA). We measure the azimuthal velocity component by focusing two beams in the radial–azimuthal plane. We correct for curvature effects of the outer cylinder by using a ray tracer (see Huisman, van Gils & Sun 2012*a*). The velocities are measured at mid-height ($z = L/2$) unless specified otherwise. For every measurement position, we measured for long enough to have a statistically stationary result, for which $\sim 10^5$ samples were required for every data point. This ensured a statistical convergence of $< 1\,\%$.

4. Global response: torque

In this section, the global response of the TC system for the four simulated radius ratios is presented. This is done by measuring the scaling law(s) of the non-dimensional torque Nu_ω as function(s) of Ta. The transition between different types of local scaling laws in different Ta ranges is investigated, and related to previous simulations (Ostilla *et al.* 2013) and experiments (van Gils *et al.* 2012).

4.1. *Pure inner cylinder rotation*

The global response of the system is quantified by Nu_ω. By definition, for purely azimuthal laminar flow, $Nu_\omega = 1$. Once the flow is driven stronger than a certain critical Ta, large azimuthal roll structures appear, which enhance angular transport through a large-scale wind.

Figure 4 shows the response of the system for increasing Ta in the case of pure inner cylinder rotation for four values of η. Experimental and numerical results are shown in the same panels, covering different ranges, and thus are complementary to, but consistent with, each other. Numerical results for $\eta = 0.714$ from Ostilla-Mónico *et al.* (2014) have been added to both panels.

As has already been noticed in Ostilla *et al.* (2013) for $\eta = 0.714$, a change in the local scaling law relating Ta to Nu_ω occurs at around $Ta \approx 3 \times 10^6$. We can interpret these changes in the same way as Ostilla *et al.* (2013) and relate the transition in the Ta–Nu_ω local scaling law to the break-up of coherent structures. A large jump in Nu_ω can be seen around $Ta \approx 5 \times 10^6$ for $\eta = 0.909$, which corresponds to a change in the number of rolls. The system goes from two pairs of rolls to three pairs of rolls.

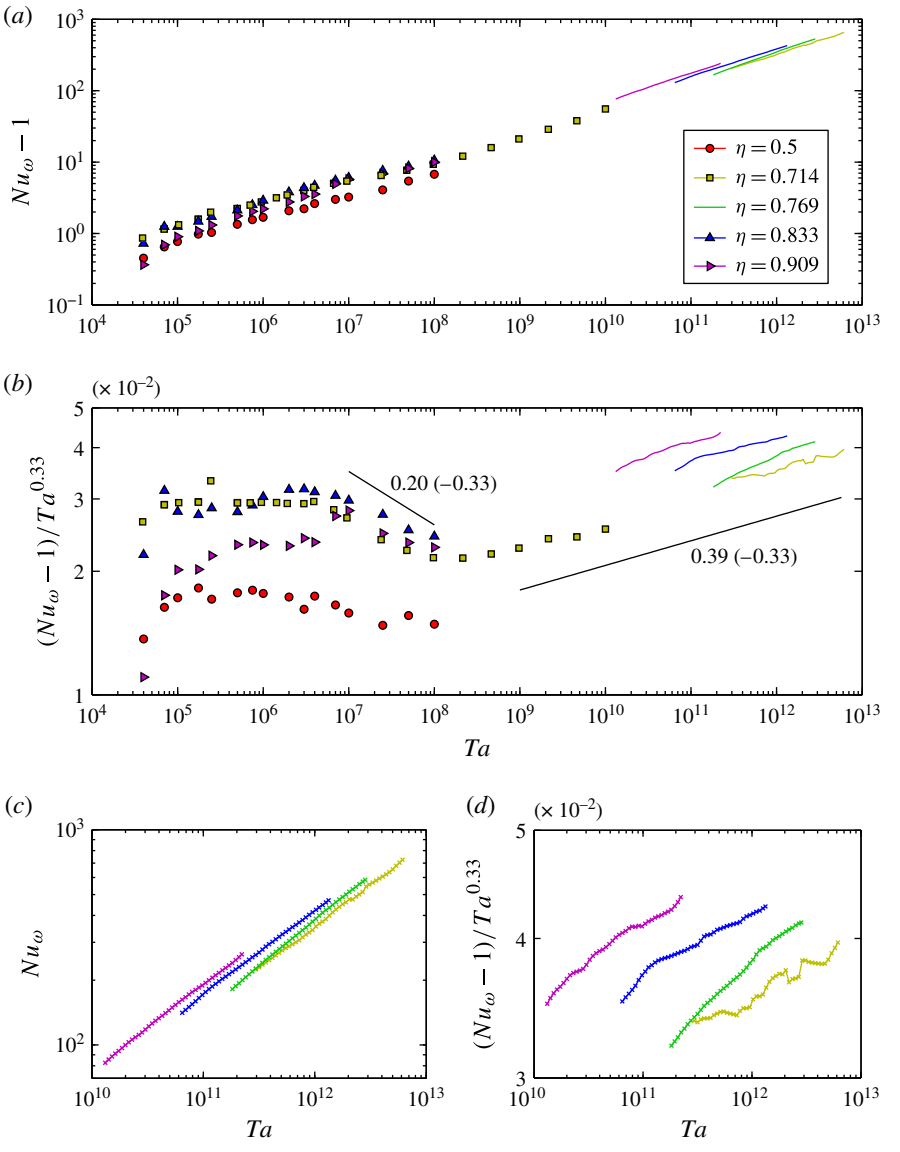

FIGURE 4. The global system response for pure inner cylinder rotation as a function of the driving Ta. (*a*) Plot of $Nu_\omega - 1$ versus Ta for both simulations (points on the left of the graph) and experiments (lines on the right of the graph). Numerical data from Ostilla-Mónico *et al.* (2014) for $\eta = 0.714$ have been added to these figures. (*b*) Plot of the compensated Nusselt number $(Nu_\omega - 1)/Ta^{1/3}$ versus Ta, with added lines with scaling law $Ta^{0.20}$ and $Ta^{0.39}$ to guide the eye. (*c*,*d*) Zoom-in of the experimental data.

It is also worth mentioning that the exponent in the local scaling laws in the regime before the transition depends on the radius ratio. This can be seen in the compensated plot, and explains the curve crossings that we see in the graphs.

For experiments (solid lines of figure 4), a different local scaling law can be seen. In this case the experiments are performed at much higher Ta than the simulations. The scaling $Nu_\omega \sim Ta^{0.38}$ can be related to the so-called 'ultimate' regime, a regime where

the boundary layers have become completely turbulent (Grossmann & Lohse 2011, 2012; Huisman *et al.* 2013). As indicated for the case at $\eta = 0.714$ we expect that for increasing Ta also the simulations become turbulent enough to reach this scaling law (cf. Ostilla-Mónico *et al.* 2014). In this regime, the local scaling law relating Ta and Nu_ω has no dependence on η and thus is universal.

In the experiments with large Ta, the value of η corresponding to the smallest gap, i.e. $\eta = 0.909$, has the highest angular velocity transport (Nu_ω) at a given Ta. This can be phrased in terms of the pseudo-Prandtl number σ, introduced in EGL07. As a smaller gap means a smaller σ, we thus find a decrease of Nu_ω with increasing σ, for the drivings explored in experiments, similarly as predicted (Grossmann & Lohse 2001) and found (Xia, Lam & Zhou 2002) for $Nu(Pr)$ in RB convection for $Pr > 1$.

4.2. *Rossby-number dependence*

In this subsection, the effect of outer cylinder rotation on angular velocity transport will be studied. Previous experimental and numerical work at $\eta = 0.714$ (van Gils *et al.* 2011*b*; Paoletti & Lathrop 2011; Brauckmann & Eckhardt 2013*a*; Ostilla *et al.* 2013) revealed the existence of an optimum transport where, for a given Ta, the transport of momentum is highest at a Rossby number Ro_{opt}^{-1}, that depends on Ta and saturates around $Ta \sim 10^{10}$. In this subsection, this work will be extended to the other values of η.

Figure 5 shows the results of the numerical exploration of the Ro^{-1} parameter space between $Ta = 4 \times 10^4$ and $Ta = 2.5 \times 10^7$. The shape of the $Nu_\omega = Nu_\omega(Ro^{-1})$ curves and the position of Ro_{opt}^{-1} depend very strongly on η in the Ta range studied in numerics. For the largest gap (i.e. $\eta = 0.5$), the optimum can be seen to be in the counter-rotating range (i.e. $Ro^{-1} < 0$) as long as Ta is high enough. On the other hand, for the smallest gap (i.e. $\eta = 0.909$), the optimum is at co-rotation (i.e. $Ro^{-1} > 0$) in the whole region studied. The other values of studied η reveal an intermediate behaviour. Optimum transport is located for co-rotation at lower values of Ta and slowly moves towards counter-rotation. For all values of η, when the driving is increased, Ro_{opt}^{-1} tends to shift to more negative values.

For two values of Ta ($Ta = 4 \times 10^6$ and $Ta = 10^7$) for a radius ratio $\eta = 0.5$, two distinct peaks can be seen in the $Nu_\omega(Ro^{-1})$ curve. This can be understood by looking at the flow topology. For $Ro^{-1} = 0$, three distinct rolls can be seen. However, when decreasing Ro^{-1}, the rolls begin to break up. Some remnants of large-scale structures can be seen, but these are weaker than in the $Ro^{-1} = 0$ case. Having a large-scale roll helps the transport of angular momentum, leading to the peak in Nu_ω at $Ro^{-1} = 0$. Further increasing the driving causes the rolls to also break up for $Ro^{-1} = 0$, and eliminates the anomalous peak.

The shift seen in the numerics may or may not continue with increasing Ta. The experiments conducted explore a parameter space of $10^{10} < Ta < 10^{13}$ and thus serve to explore the shift at higher driving. Figure 6 presents the obtained results. Figure 6(*a*) shows Nu_ω versus Ta for all measurements. Figure 6(*b*) shows the exponent γ, obtained from a least-squares linear fit of the log–log plots. Across the η and Ro^{-1} ranges studied, the average exponent is $\gamma \approx 0.39$. This value is used in figure 7 to compensate Nu_ω. The horizontality of all data points reflects the good scaling and the universality of this ultimate scaling behaviour $Nu_\omega \propto Ta^{0.39}$.

To determine the optimal rotation ratio for the experimental data, a Ta-averaged compensated Nusselt number $\langle Nu_\omega / Ta^{0.39} \rangle_{Ta}$ was used. This is defined as

$$\langle Nu_\omega / Ta^{0.39} \rangle_{Ta} = \frac{1}{Ta_{max} - Ta_{co}} \int_{Ta_{co}}^{Ta_{max}} \frac{Nu_\omega}{Ta^{0.39}} \, \mathrm{d}Ta, \tag{4.1}$$

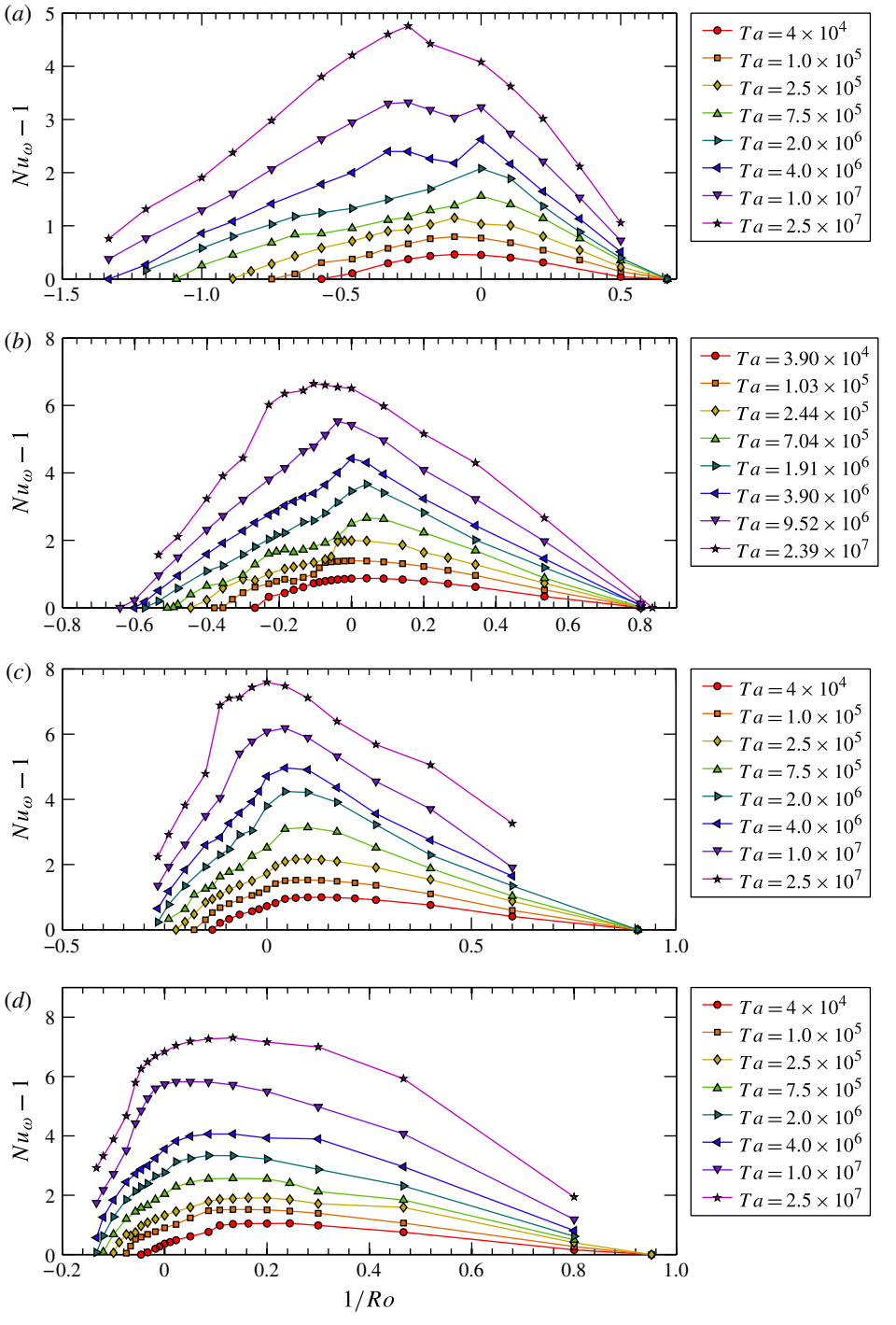

FIGURE 5. (Colour online) Plots of $Nu_\omega - 1$ versus Ro^{-1} for the four values of η studied numerically: (*a*) $\eta = 0.5$, (*b*) $\eta = 0.714$, (*c*) $\eta = 0.833$ and (*d*) $\eta = 0.909$. The shape of the curve and the position of the maximum depend very strongly on both Ta and η.

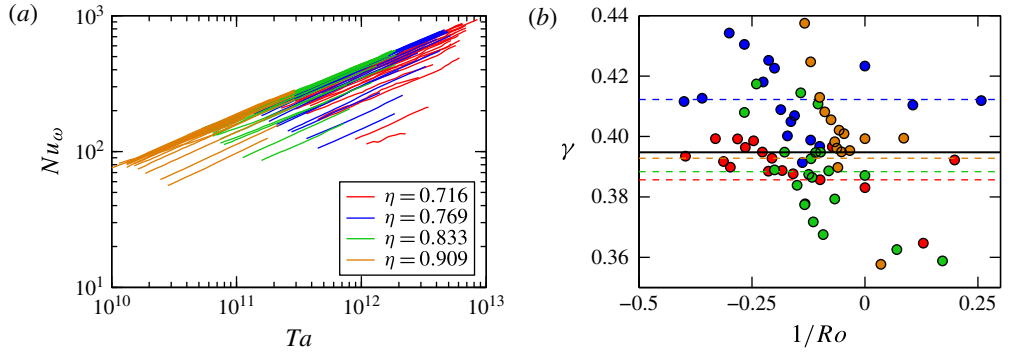

FIGURE 6. (*a*) Plot of Nu_ω versus Ta for all values of η and Ro^{-1} studied in the experiments. (*b*) The exponent γ of the scaling law $Nu_\omega \propto Ta^\gamma$ for various Ro^{-1}, obtained by a least-squares linear fit in log–log space. Red circles are data for $\eta = 0.716$, blue circles for $\eta = 0.769$, green circles for $\eta = 0.833$ and yellow circles for $\eta = 0.909$. The average value of γ for each η is represented by the dashed lines, while the solid line represents the average value of $\gamma = 0.39$ for all η, which will be used for compensating Nu_ω.

where Ta_{max} is the maximum value of Ta for every (η, Ro^{-1}) dataset, and Ta_{co} is a cut-off Ta number used for larger η ($Ta_{co} = 2 \times 10^{11}$ for $\eta = 0.833$, and $Ta_{co} = 3 \times 10^{10}$ for $\eta = 0.909$) to exclude the initial part of the $Nu_\omega/Ta^{0.39}$ data points, which seem to have a different scaling for some of the values of Ro^{-1} explored. For the smaller values of η, we have $Ta_{co} = Ta_{min}$, the minimum value of Ta for every (η, Ro^{-1}) dataset. An error bar on this average is estimated as one standard deviation of the data from the computed average.

Figure 8(*a*,*b*) shows $\langle Nu_\omega/Ta^{0.39}\rangle_{Ta}$ as a function of Ro^{-1} or alternatively of a for the four values of η considered in experiments. The increased driving changes the characteristics of the flow. This is reflected in the very different shapes of the Ro^{-1} dependence of Nu_ω when comparing figures 5 and 8, and in the shift of Ro^{-1}_{opt}.

To summarize these effects, figure 9 presents both the 95 % peak width ΔRo^{-1}_{max} and the position of optimal transport Ro^{-1}_{opt} determined as the realization with the maximum torque as a function of Ta and η obtained from numerics as well as the asymptotic value from experiments. The peak width ΔRo^{-1}_{max} is defined as

$$\Delta Ro^{-1}_{max} = \frac{\displaystyle\int_{Ro^{-1}_{-0.95}}^{Ro^{-1}_{0.95}} Nu_\omega(Ro^{-1})\,\mathrm{d}Ro^{-1}}{\max(Nu_\omega - 1)}, \tag{4.2}$$

where $Ro^{-1}_{-0.95}$ and $Ro^{-1}_{0.95}$ are the values of Ro^{-1} for which Nu_ω is 95 % of the peak value.

The 95 % peak width can be seen to vary with driving, reflecting what is seen in figure 5. The shape of the Ro^{-1}–Nu_ω curve is highly dependent on both η and Ta. Also, Ro^{-1}_{opt} shows a very large variation across the Ta range studied in numerics. The shift of Ro^{-1}_{opt} with Ta is expected to continue until it reaches the value found in the experiments. This can be seen in figure 5 for $\eta = 0.5$ to $\eta = 0.833$. For $\eta = 0.909$, the

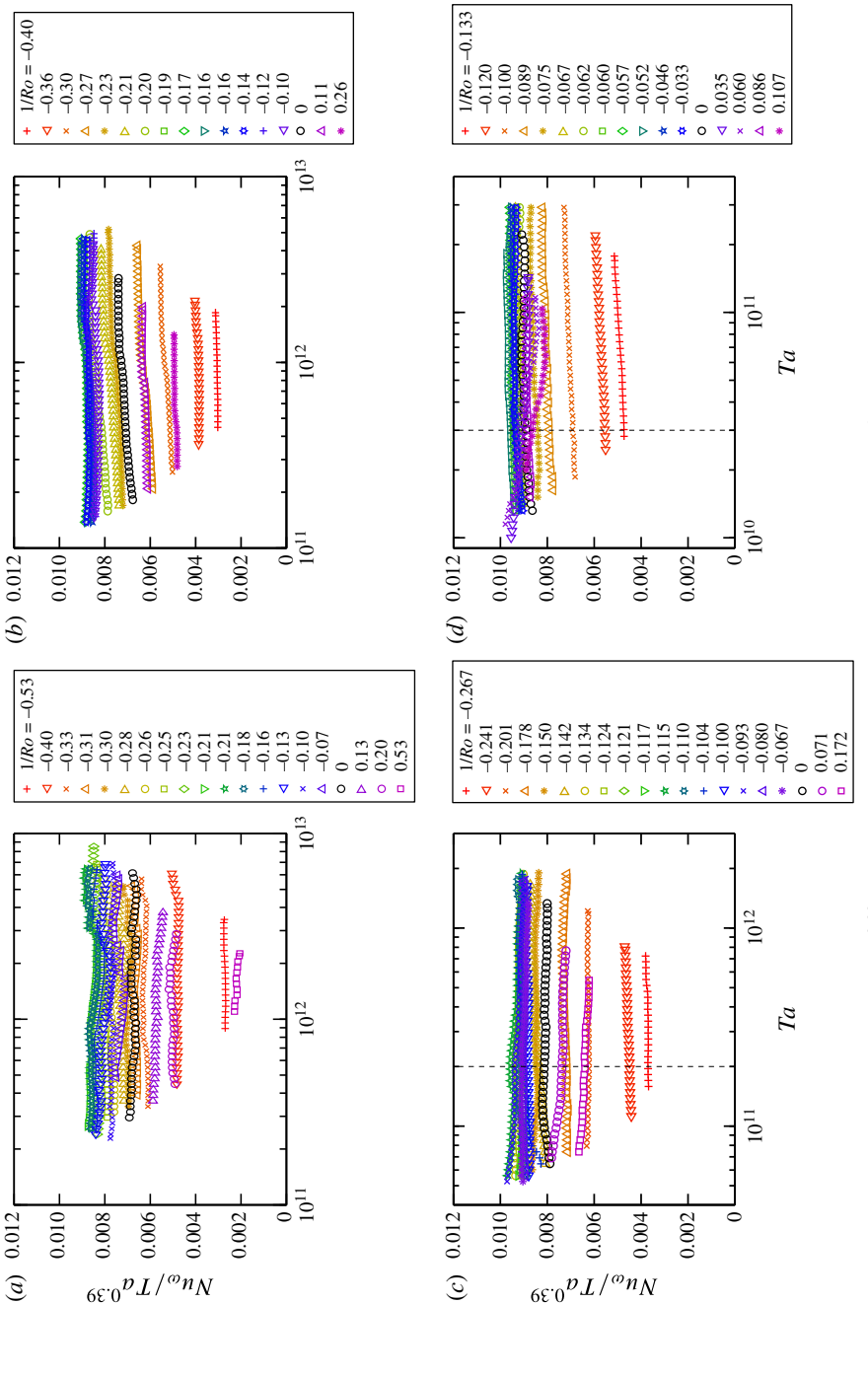

FIGURE 7. (Colour online) Plots of $Nu_\omega/Ta^{0.39}$ versus Ta for all explored values of Ro^{-1} for the four studied values of η: (*a*) $\eta = 0.716$, (*b*) $\eta = 0.769$, (*c*) $\eta = 0.833$ and (*d*) $\eta = 0.909$. The scaling law $Nu_\omega \sim Ta^{0.39}$ is seen to hold approximately throughout the whole parameter space explored. No trends can be appreciated that would lead us to expect further shift of the optimum with increased driving. Dashed lines, indicating the cut-off regions used for determining $\langle Nu_\omega/Ta^{0.39}\rangle_{Ta}$, have been plotted for $\eta = 0.833$ and $\eta = 0.909$.

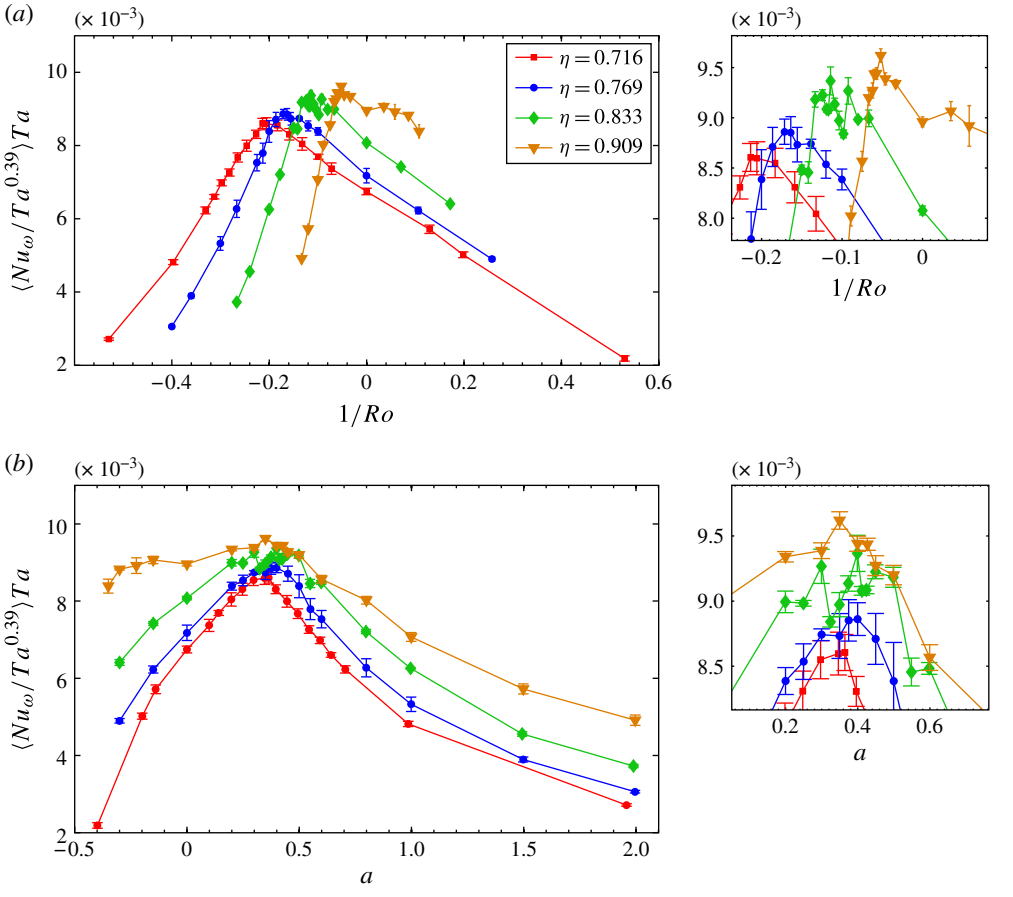

FIGURE 8. (Colour online) Plots of $\langle Nu_\omega/Ta^{0.39}\rangle_{Ta}$ versus either (*a*) Ro^{-1} or (*b*) a at the cut-off region highlighted in figure 7 for the values of η studied experimentally. The smaller right-hand panels show a zoom-in around the optimum, and have been added for clarity. Error bars indicate one standard deviation from the mean value, and are too small to be seen for most data points. There is a strong η dependence of the curve $Nu_\omega/Ta^{0.39}$ versus Ro^{-1}, even at the largest drivings studied in the experiments. Optimal transport is located at $Ro_{opt}^{-1} = -0.20$ for $\eta = 0.716$, $Ro_{opt}^{-1} = -0.15$ for $\eta = 0.769$, $Ro_{opt}^{-1} = -0.10$ for $\eta = 0.833$ and $Ro_{opt}^{-1} = -0.05$ for $\eta = 0.909$, corresponding to $a \approx 0.33$–0.35 for all values of η. In panel (*b*) the maximum of the graph is less pronounced, i.e. it becomes flatter with increasing η. In the limit $\eta \to 1$, a does not tend to a finite limit, while Ro^{-1} does. This result highlights the advantage of using Ro^{-1} instead of a as a control parameter.

trend seems to change for the last point. However, this is due to the very large and flat peak of the $Nu_\omega(Ro^{-1})$ curve – this can also be seen in the left panel of figure 9 and in figure 5(*d*).

One may also ask the question: has the value of Ro_{opt}^{-1} already saturated in our experiments? Figure 7 shows the trend for Nu_ω for increasing Ta. This trend does not seem to vary much for different values of Ro^{-1}. Therefore, we expect the value of Ro_{opt}^{-1} to have already reached saturation in our experiments.

We can compare these new experimental results to the available results from the literature, the speculation made in van Gils *et al.* (2012) and the prediction made in

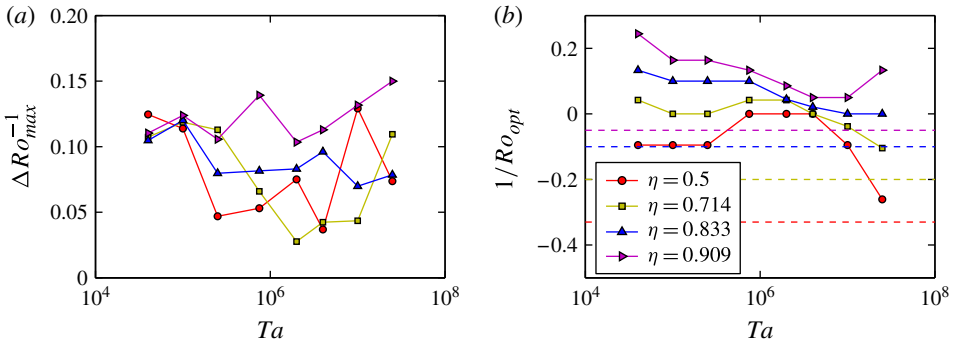

FIGURE 9. (Colour online) (*a*) The 95 % peak width ΔRo_{max}^{-1} versus Ta for the four values of η analysed in numerics. The peak width can be seen to vary with driving, and for smaller gaps is larger for larger values of Ta. (*b*) Plot of Ro_{opt}^{-1} versus Ta for the same four values of η. The location of the optimal transport has a very strong dependence on the driving, especially for the largest values of η. As driving increases beyond the numerically studied range and overlaps with experiments, Ro_{opt}^{-1} should tend to the experimentally found values, represented as dashed lines. The asymptote for $\eta = 0.5$ is obtained from Merbold *et al.* (2013). The trend appears to be less clear for $\eta = 0.909$, but this might be understandable from the peak width at the highest driving Ta.

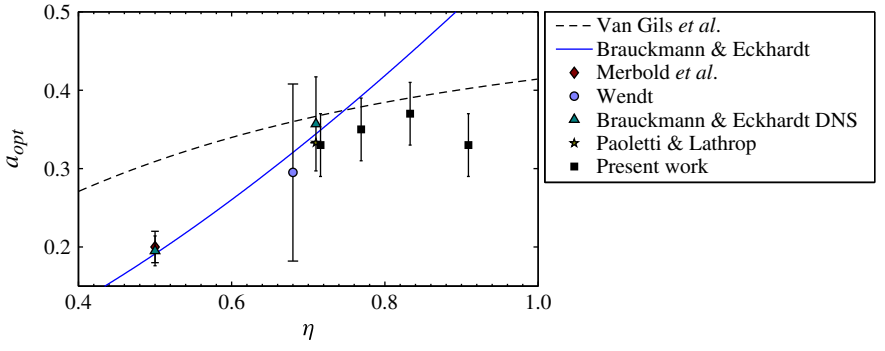

FIGURE 10. (Colour online) State-of-the-art data for $a_{opt}(\eta)$, from both experiments (Wendt 1933; Paoletti & Lathrop 2011; Merbold *et al.* 2013) and numerics (Brauckmann & Eckhardt 2013*b*). The speculation of van Gils *et al.* (2012) and the prediction of Brauckmann & Eckhardt (2013*b*) are plotted as lines on the graph. The new experimental results deviate substantially from both predictions, even when taking into account error bars.

Brauckmann & Eckhardt (2013*b*) for the dependence of the saturated a_{opt} on η. This is shown in figure 10. Error bars are either taken from the literature, or computed by fitting a quadratic polynomial to $Nu_\omega(a)$ for three values of a below the maximum, i.e. $a < a_{opt}$, three values of a after the maximum, i.e. $a > a_{opt}$, and the six values of a, and comparing the different results obtained. Both dependences are shown to deviate substantially from the experimental results obtained in the present work. Even if the speculation from van Gils *et al.* (2012) appears to be better for this η range, for previous experimental data at $\eta = 0.5$, it is clearly different from the experimentally measured value for optimal transport by Merbold *et al.* (2013).

This section has shown that the radius ratio has a very strong effect on the global response and especially on optimal transport. Significantly increased transport for co-rotation has been found at the lowest drivings based on the DNS results. This finding was already reported in Ostilla *et al.* (2013) for $\eta = 0.714$, but the transport increase was marginal. For $\eta = 0.833$, and especially for $\eta = 0.909$, the transport can be increased up to three times. The shift of Ro_{opt}^{-1} has also been seen to be much bigger and to happen in a much slower way for smaller gaps. The reason for this will be studied in § 5, using the local data obtained from experiments and numerics.

5. Local results

In this section, the local angular velocity profiles will be analysed. Angular velocity is the transported quantity in TC flow and shows the interplay between the bulk, where the transport is convection-dominated, and the boundary layers, where the transport is diffusion-dominated. Numerical profiles and experimental profiles obtained from LDA will be shown. The angular velocity gradient in the bulk will be analysed and connected to the optimal transport. In addition, the boundary layers will be analysed and compared to the results from the analytical formula from EGL07 for the BL thickness ratio in the non-ultimate regime.

5.1. *Angular velocity profiles*

Angular velocity ω profiles obtained from numerics are shown in figure 11. Results are presented for four values of η and selected values of Ro^{-1} at $Ta = 2.5 \times 10^7$ (and $Ta = 2.39 \times 10^7$ for $\eta = 0.714$). Experimental data obtained by using LDA are shown in figure 12 for three values of η: (*a*) $\eta = 0.714$ for $Re_i - Re_o = 10^6$, (*b*) $\eta = 0.833$ for $Ta = 5 \times 10^{11}$, and (*c*) $\eta = 0.909$ for $Ta = 1.1 \times 10^{11}$.

The different radius ratios affect the angular velocity profiles on both boundary layers, as the two boundary layers are more asymmetric for wide gaps; and they affect the bulk, as the bulk angular velocity is smaller for wide gaps. These effects will be analysed in the next sections.

5.2. *Angular velocity profiles in the bulk*

We now analyse the properties of the angular velocity profiles in the bulk. We find that the slope of the profiles in the bulk is controlled mainly by Ro^{-1} and less so by Ta. This can be understood as follows. The Taylor number Ta acts through the viscous term, dominant in the boundary layers, while Ro^{-1} acts through the Coriolis force, present in the whole domain. These results extend the finding from Ostilla *et al.* (2013) to other values of η.

To further quantify the effect of Ro^{-1} on the bulk profiles, we calculate the gradient of $\langle \bar{\omega} \rangle_z$. For the DNS data, this is done by numerically fitting a tangent line to the profile at the inflection point using the two neighbouring points on both sides (at a distance of 0.01–0.02 r units); such a fit is shown in figure 13(*a*).

As the spatial resolution of the LDA data is more limited, the fit is done differently. A linear regression to the ω profile between $0.2 < \tilde{r} < 0.8$ is carried out. The larger range of $\tilde{r}$ is chosen in experiments because: (i) the boundary layers are small enough due to the high Ta that they are outside of the fitting range, and (ii) the fluctuations of the data are much higher in experiments, especially for the LDA of the narrow gaps ($\eta = 0.833$ and $\eta = 0.909$). From this regression, we calculate $\langle \bar{\omega} \rangle_z$, and an error taken from the covariance matrix of the fit.

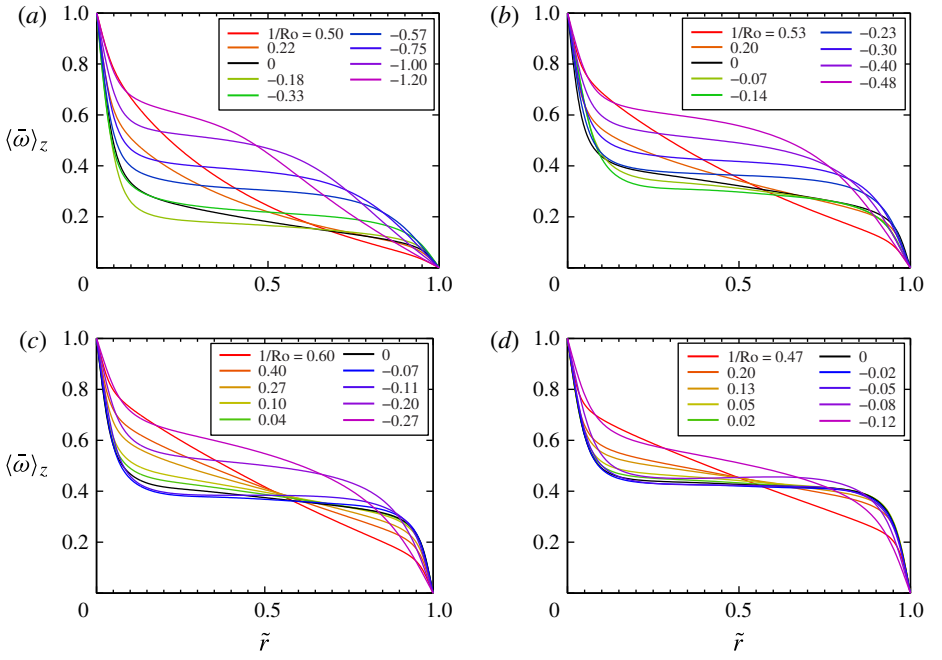

FIGURE 11. Azimuthally, axially and temporally averaged angular velocity $\langle\bar{\omega}\rangle_z$ versus radius $\tilde{r}$ for: (*a*) $\eta = 0.5$, (*b*) $\eta = 0.714$, (*c*) $\eta = 0.833$ and (*d*) $\eta = 0.909$. Data are for $Ta = 2.5 \times 10^7$ ($Ta = 2.39 \times 10^7$ for $\eta = 0.714$) and selected values of Ro^{-1}. For smaller η, the ω bulk profiles differ more from a straight line, and have, on average, a smaller value.

Figure 14 shows four panels, each containing the angular velocity gradient in the bulk from the numerical simulations and experiments for a given value of η. We first notice that the angular velocity gradients from experiment and numerics are in excellent agreement. Next the connection between a flat angular velocity profile and optimal transport for the highest drivings explored in the experiments can now be seen for other values of η and not just for $\eta = 0.714$ as reported previously (van Gils *et al.* 2011*b*). Once $Ro^{-1} < Ro_{opt}^{-1}$, the large-scale balance analysed in Ostilla *et al.* (2013) breaks down, and a 'neutral' surface that reduces the transport appears in the flow.

In simulations, because of resolution requirements, we are unable to drive the flow strongly enough to see a totally flat bulk profile. Also, the influence of the large-scale structures causes a small discrepancy between the flattest profile and the value of Ro_{opt}^{-1} measured from Nu_ω. This is expected to slowly disappear with increasing Ta.

In Ostilla *et al.* (2013), a linear extrapolation of the bulk angular velocity gradient was made to give an estimate for the case when this profile would become horizontal, i.e. $\mathrm{d}\langle\bar{\omega}\rangle_z/\mathrm{d}\tilde{r} = 0$, and thus give an estimate of Ro_{opt}^{-1}. For $\eta = 0.714$ this estimate agreed with the numerical result within error bars. Here, we extend this analysis for the other values of η and, as we shall see, successfully.

As in Ostilla *et al.* (2013), an almost linear relationship between Ro^{-1} and $\mathrm{d}\langle\bar{\omega}\rangle_z/\mathrm{d}\tilde{r}$ can be seen. This linear relationship is extrapolated and plotted in each panel. This extrapolation gives an estimate for $Ro_{opt}^{-1}(Ta \to \infty)$, which we can compare to the experimentally determined $Ro_{opt}^{-1}(Ta \to \infty)$. For $\eta = 0.833$, $Ro^{-1}(Ta \to \infty) \approx -0.12$, corresponding to $a \approx 0.38$, is obtained; and for $\eta = 0.909$, $Ro^{-1}(Ta \to \infty) \approx -0.05$, corresponding to $a \approx 0.31$, is obtained. These values are (within error bars) also

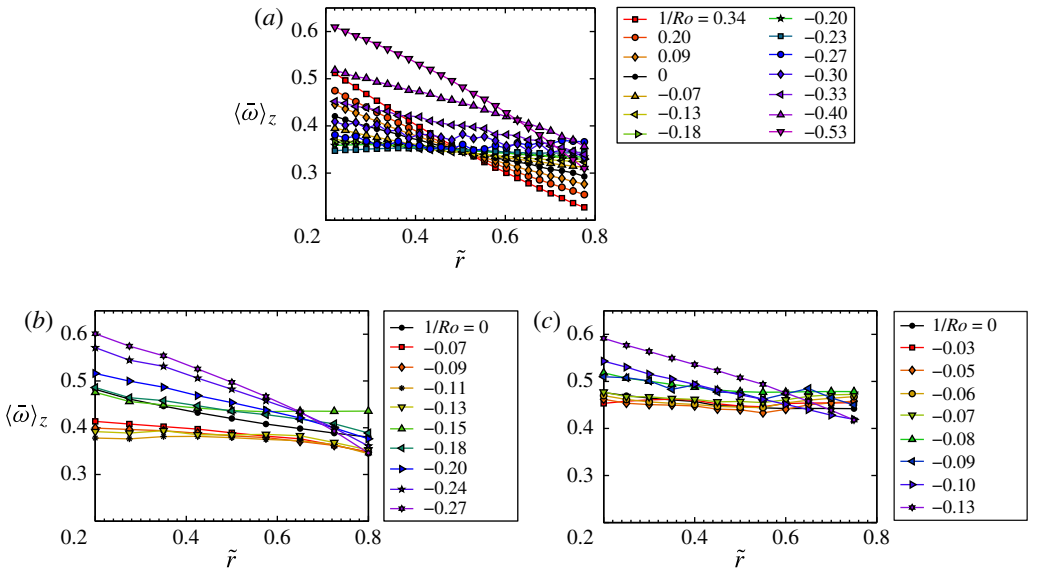

FIGURE 12. (Colour online) Angular velocity profiles obtained by LDA for either (*a*) $\eta = 0.716$ at $Re_i - Re_o = 10^6$, (*b*) $\eta = 0.833$ at $Ta = 5 \times 10^{11}$ and (*c*) $\eta = 0.909$ at $Ta = 1.1 \times 10^{11}$, to explore different dependences in parameter space. Data are taken at a fixed axial height (i.e. the cylinder mid-height, $z = L/2$), but as the Taylor number Ta is much larger than in the numerics, the axial dependence is much weaker.

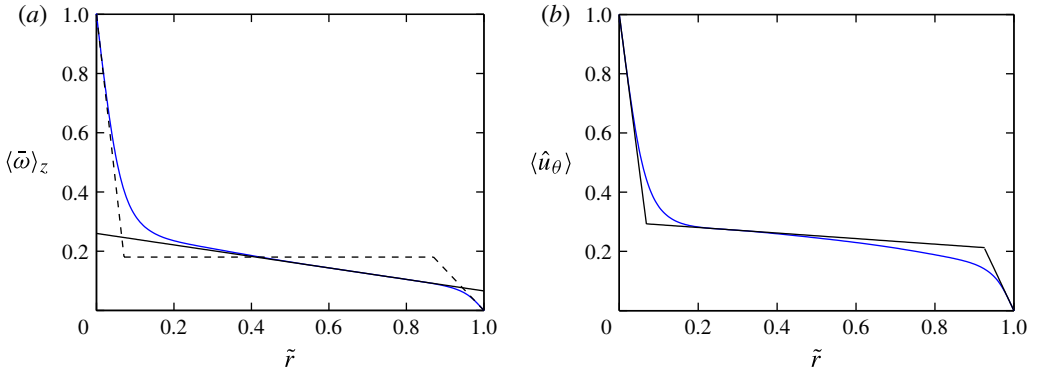

FIGURE 13. (Colour online) An example of the two fitting procedures for the bulk angular velocity gradient and for boundary layer thicknesses done on the DNS data. The two panels show the θ-, z- and t-averaged azimuthal velocity and angular velocity for $\eta = 0.5$, $Ta = 1 \times 10^7$, and pure inner cylinder rotation. (*a*) A line is fitted to the bulk of the angular velocity to obtain the bulk gradient. The dashed lines indicate the EGL07 approximation. (*b*) The three-line fit to the whole profile to obtain the width of its boundary layers, used in § 5.3. Both bulk fits are done at the inflection point, but for different variables ($\bar{\omega}$ or $\bar{u}_\theta$), which gives slightly different slopes (and intersection points).

obtained for Ro_{opt}^{-1} at the large Ta investigated in experiments, namely $Ro_{opt}^{-1} = -0.10$ and -0.05, respectively.

For $\eta = 0.5$, $Ro_{opt}^{-1}(Ta \to \infty) \approx -0.33$ is obtained, corresponding to $a \approx 0.2$. This value is consistent with the numerical results in Brauckmann & Eckhardt (2013*b*),

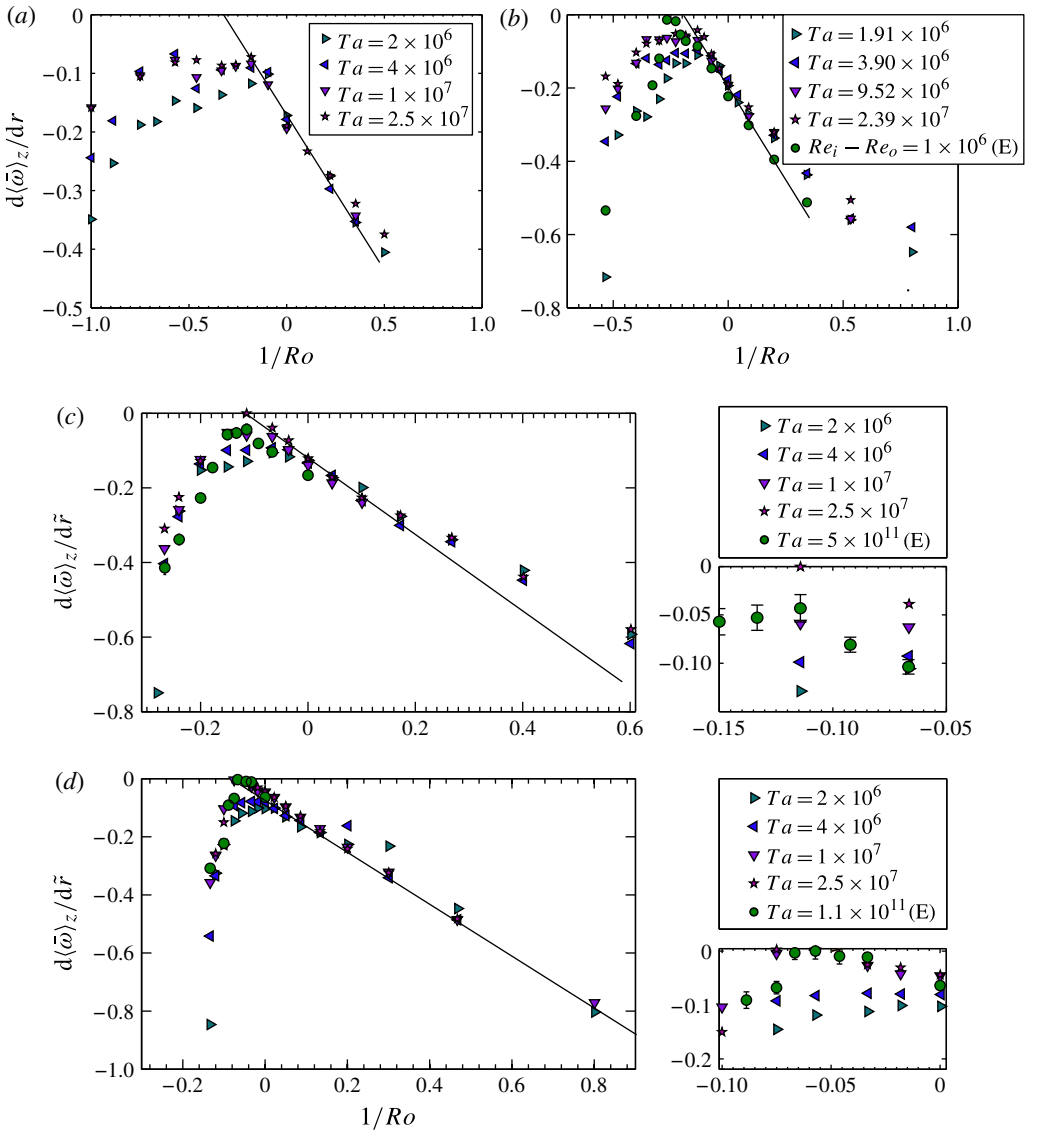

FIGURE 14. (Colour online) Bulk angular velocity gradient $\mathrm{d}\langle\bar{\omega}\rangle_z/\mathrm{d}\tilde{r}$ against Ro^{-1} for the four values of η explored in simulations: (*a*) $\eta = 0.5$, (*b*) $\eta = 0.714$, (*c*) $\eta = 0.833$ and (*d*) $\eta = 0.909$. Data from experiments obtained by LDA are also plotted for the three values of η for which it was experimentally measured (green circles). For all values of η except $\eta = 0.5$, for co-rotation and slight counter-rotation, there is once again an almost linear relationship between Ro^{-1} and $\mathrm{d}\langle\bar{\omega}\rangle_z/\mathrm{d}\tilde{r}$. A black straight line is added to extrapolate this relationship in order to estimate Ro_{opt}^{-1}. A plateau, in which the radial gradient of $\langle\bar{\omega}\rangle_z$ is small, can be seen around optimal transport, indicating a large convective transport of angular velocity.

which report $a_{opt} \approx 0.2$. However, care must be taken, as fitting straight lines to the ω profiles gives higher residuals for $\eta = 0.5$ as the profiles deviate from straight lines (cf. figure 11*a*). A fit to the 'quarter-Couette' profile derived from upper bound theory (Busse 1967) is much more appropriate for $\eta = 0.5$ at the strongest drivings achieved

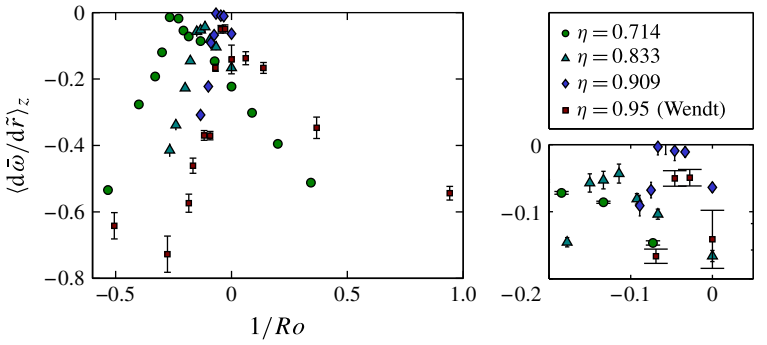

FIGURE 15. (Colour online) Bulk angular velocity gradient $d\langle\bar{\omega}\rangle_z/d\tilde{r}$ against Ro^{-1} for the three values of η explored in experiments, and for $\eta = 0.95$ (digitized from Wendt (1933)). The error bars of Wendt's data are larger due to the quality of the digitization. As seen previously, the flattest profile occurs around weak counter-rotation, for all values of η, including $\eta = 0.95$.

in experiments (Merbold *et al.* 2013). This is because the flow feels much more the effect of the curvature at small η. At the other end of the scale, the linear relationship works best for the smallest gaps, i.e. $\eta = 0.909$ (cf. figure 11*d*), where curvature plays a small effect.

To further elaborate the link between η, flat ω profiles and Ro^{-1}, data for the smallest gap $\eta = 0.95$ from Wendt (1933) has been digitized, and $d\langle\bar{\omega}\rangle_z/d\tilde{r}$ has been determined for it. These data correspond to a driving of $Ta \sim 10^8$–10^9. Figure 15 shows $d\langle\bar{\omega}\rangle_z/d\tilde{r}$ against Ro^{-1} for Wendt's data and also for the current experimental data. The flattest profile can be seen to occur for increasing (in absolute value) Ro^{-1} for larger gaps, similar to the shift of Ro^{-1}. For $\eta = 0.95$, almost no curvature is felt by the flow and flat profiles can be seen for $-0.05 < Ro^{-1} < 0$. However, adding a Coriolis force (in the form of Ro^{-1}), a large ω gradient is sustained in the bulk. This corroborates the balance between Ro^{-1} and the bulk ω gradients proposed in Ostilla *et al.* (2013).

5.3. *Angular velocity profiles in the boundary layers in the classical turbulent regime*

As the driving is increased, the transport is enhanced. To accommodate this, the boundary layers (BLs) become thinner and therefore the ω slopes ($\partial_r\omega$) become steeper. Owing to the geometry of the TC system, an intrinsic asymmetry in the BL layer widths is present. More precisely, the exact relationship $\partial_r\langle\omega\rangle|_o = \eta^3\partial_r\langle\omega\rangle|_i$ holds for the slopes of the boundary layers, due to the r independence of J^ω (EGL07 and (2.4)).

An analysis of the boundary layers was not possible in the present experiments because the present LDA measurements have insufficient spatial resolution to resolve the flow in the near-wall region. Therefore, only DNS results will be analysed here. In simulations the driving is not as large as in experiments, and as a consequence the shear in the BLs is expected to be not large enough to cause a shear instability. This means that the BLs are expected to be of Prandtl–Blasius (i.e. laminar) type, even if the bulk is turbulent. On the other hand, in the experiments both boundary layers and bulk are turbulent, i.e. the system is in the 'ultimate regime'.

Using the DNS data, we can compare the ratio of the numerically obtained boundary layer widths with the analytical formula for this ratio obtained by EGL07 for laminar boundary layers, namely

$$\frac{\lambda_\omega^o}{\lambda_\omega^i} = \eta^{-3}\frac{|\omega_o - \omega_{bulk}|}{|\omega_i - \omega_{bulk}|}, \tag{5.1}$$

where the value of ω_{bulk} is some appropriate value in the range from which the angular velocity at the inflection point of the profile might be chosen, i.e. the point at which the linear bulk profile fit was done to obtain λ_ω^o and λ_ω^i. The value ω_{bulk} is taken from the numerics, and may bias the estimate.

To calculate the boundary layer thicknesses, the profile of the mean azimuthal velocity $\langle \bar{u}_\theta \rangle_z$ is approximated by three straight lines, one for each boundary layer and one for the bulk. For the boundary layers the slope of the fit is calculated by fitting (by least-mean-squares) a line through the first two computational grid points. For the bulk, first the line is forced to pass through the grid point that is numerically closest to the inflection point of the profile. Then its slope is taken from a least-mean-squares fit using two grid points on both sides of this inflection point. The respective boundary layer line will cross this bulk line at a point that then defines the thickness of that boundary layer.

The results obtained for $\lambda_\omega^o/\lambda_\omega^i$ both from (5.1) and directly from the simulations are shown in figure 14. Results are presented for the four values of η and only for the highest value of Ta achieved in the simulations. The boundary layer asymmetry for counter-rotating cylinders (i.e. $Ro^{-1} < 0$) grows with larger gaps. This is to be expected, as the η^{-3} term is much larger ($\approx$8) for the largest gap as compared to the smallest gap ($\approx$1.3). This is consistent with the η and thus σ restriction in EGL07 to a range of smaller gap widths.

As noted already in Ostilla *et al.* (2013) we find that the fit is not satisfactory for co-rotation (i.e. $Ro^{-1} > 0$) at the lowest values of η, but is satisfactory for counter-rotation (i.e. $Ro^{-1} < 0$). In EGL07, equation (5.1) is obtained by approximating the profile by three straight lines, two for the BLs and a constant ω line for the bulk. Therefore, we expect the approximation to hold best when the bulk has a flat gradient. For co-rotating cylinders and strongly counter-rotating cylinders, the bulk has a steep gradient (see figure 14), but characteristically different shapes. The only free parameter in (5.1) is ω_{bulk}, which is chosen to be ω at the point of inflection. owing to the different shapes of the ω profiles, this choice seems more correct for counter-rotating cylinders, as there is a clear inflection point in the profile. On the other hand, for co-rotating cylinders, the profile appears to be more convex-like, and there the choice of ω_{bulk} as the inflection point induces errors in the approximation (cf. figure 13*a*). For $\eta = 0.5$, the error from the constant-ω approximation is even more pronounced, and the formula fails.

For co-rotation the boundary layers are approximately of the same size, and the ratio $\lambda_\omega^o/\lambda_\omega^i$ is very close to 1. If one inverts (5.1) by approximating this ratio by 1, an estimate of what the angular velocity will be in the bulk due to the boundary layer slope asymmetry is obtained,

$$\omega_{bulk} = \frac{\eta^3}{1+\eta^3}, \tag{5.2}$$

corresponding to

$$\omega_{bulk}^\ell = \frac{-\omega_o^\ell + \eta^3\omega_i^\ell}{1+\eta^3}, \tag{5.3}$$

in the laboratory frame. This expression gives an estimate for ω_{bulk} when the profile is flattest, and has been represented graphically in figure 11. Indeed, one can take this

estimate (e.g. 0.27 for $\eta = 0.714$) and compare it with figures 11 and 12. We note that the value of ω in the bulk for the flattest profile in the numerics (at $Ro^{-1} \approx Ro_{opt}^{-1}(Ta)$) lies around ω_{bulk}. We can also note that the profiles for $Ro^{-1} > Ro_{opt}^{-1}$ approximately cross each other at the same point, and this point has a value of $\omega \approx \omega_{bulk}$. This effect can only be seen in the numerics, as these approximations break down once the boundary layers become turbulent. The crossing points of the curves are taken as an estimate for ω_{bulk}, and this is represented against (5.2) in figure 17.

To understand why the boundary layers are of approximately the same thickness despite the different initial slopes at the cylinders, one has to go back to (2.4). The angular velocity current has a diffusive part and a convective part. Per definition, in the boundary layer the diffusion dominates, and in the bulk the convection does. Thus the boundary layer ceases when convection becomes significant. But convection is controlled by the wind. Thus in essence the boundary layer size is controlled by the wind and not immediately by the initial slope at the wall. Owing to continuity, if the rolls penetrate the whole domain the wind may be expected to be the same close to the inner and close to the outer cylinder. This suggests that the flow organizes itself in such a way that the boundary layer extensions (or widths) might be similar, even if the initial slopes at the walls are different.

What happens for counter-rotation, or more precisely when $Ro^{-1} < Ro_{opt}^{-1}$? For Ro^{-1} below the optimum Ro_{opt}^{-1}, a so-called neutral surface will be present in the flow, which separates the Rayleigh-stable and -unstable areas. The wind drastically changes in the Rayleigh-stable areas (Ostilla *et al.* 2013), leading to very different wind velocities close to the outer and inner cylinder, respectively. The wind at the outer cylinder will be weaker, as the rolls cannot fully penetrate the Rayleigh-stable domain. This means that the outer cylinder boundary layer will extend deeper into the flow, in accordance with what is seen in figure 16.

6. Summary and conclusions

Experiments and direct numerical simulations (DNS) were analysed to explore the effects of the radius ratio η on turbulent Taylor–Couette flow. Numerical results corresponding to Taylor numbers in the range of $10^4 < Ta < 10^8$ along with experiments in a Taylor number range of $10^{10} < Ta < 10^{12}$ were presented for four values of the radius ratio η.

First the influence of the radius ratio on the global scaling law $Nu_\omega \sim Ta^\gamma$ was studied. The local scaling exponent γ describing the response of the torque caused by a Taylor number increase is barely modified by varying the radius ratio η. Indeed, in experiments a universal exponent of $\gamma \approx 0.39$ is obtained, independent of radius ratio and outer cylinder rotation. For the numerical simulations at lower Ta similar universal behaviour can be observed. The transition associated with the vanishing of coherent structures can also be appreciated at $Ta \sim 10^6$ for all values of η. Before this transition local exponents of $\gamma \approx 0.33$ are seen, and after the transition these decrease to approximately $\gamma \approx 0.2$.

The radius ratio does play a very important role in optimal transport. At smaller gaps, i.e. for larger η, at the lower end of the Ta range a very large increase in transport for co-rotating cylinders can be seen. The shift towards the asymptotic optimal transport happens in a much slower way for small gaps, but this shift is seen for all studied radius ratios. For the largest gap ($\eta = 0.5$), optimal transport for pure inner cylinder rotation at the lowest drivings is obtained. The shift towards the asymptotic value happens suddenly, as two peaks can be seen in the Nu_ω versus Ro^{-1} curve, and one of the peaks becomes larger than the other one as driving increases.

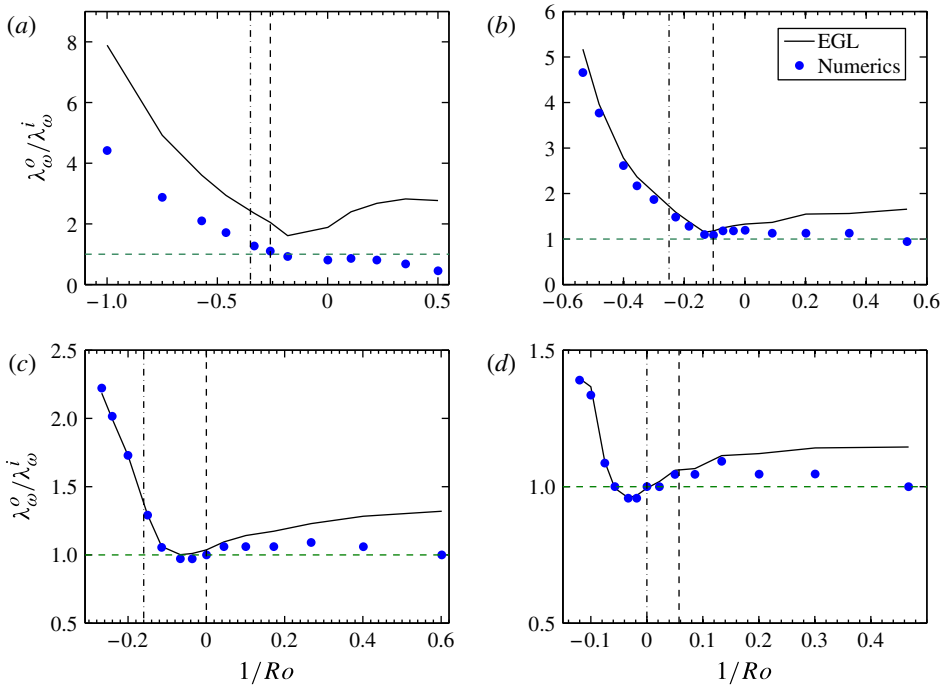

FIGURE 16. (Colour online) Plots of $\lambda_\omega^o/\lambda_\omega^i$ from simulations (circles) and from (5.1) (solid lines; EGL07) versus Ro^{-1} for the four values of η studied numerically, i.e. (*a*) $\eta = 0.5$, (*b*) $\eta = 0.714$, (*c*) $\eta = 0.833$ and (*d*) $\eta = 0.909$, at $Ta = 2.5 \times 10^7$. The numerical results and the estimate from (5.1) match very well for larger values of η and especially for counter-rotating cylinders ($1/Ro < 0$). The vertical black dashed line indicates Ro_{opt}^{-1}, while the vertical dash-dotted line indicates the 90 % peak width on the counter-rotation side. $\lambda_\omega^o/\lambda_\omega^i$ begins to deviate from one between the two lines, as counter-rotation increases. The asymmetry between the boundary layers can be seen to be larger for smaller values of η, which is expected, as (5.1) contains the explicit factor η^{-3}.

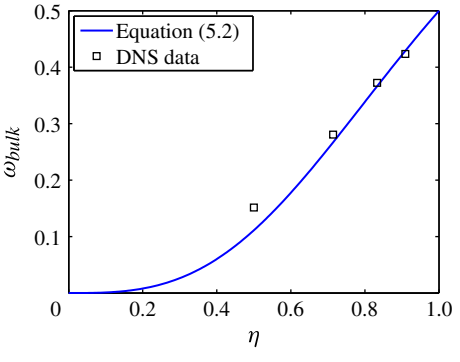

FIGURE 17. (Colour online) Plot of ω_{bulk} as a function of η, taken from both (5.2) and from the crossing points of the ω profiles in figure 11. The trend is the same in both datasets. A smaller value of η decreases the value of the bulk angular velocity.

Radius ratio, η	Extrapolated Ro_{opt}^{-1}/a_{opt}	Measured Ro_{opt}^{-1}/a_{opt}
0.5	−0.33/0.20	—/—
0.714	−0.20/0.33	−0.20/0.33
0.769	—/—	−0.20/0.36
0.833	−0.12/0.41	−0.10/0.37
0.909	−0.05/0.34	−0.05/0.34

TABLE 2. Summary of values obtained for Ro_{opt}^{-1} and a_{opt} through both the extrapolation of $\mathrm{d}\langle\bar{\omega}\rangle_z/\mathrm{d}\tilde{r}$ (§ 5.2) and direct measurement of the torque (§ 4.2) for the various values of η studied in this paper.

This might point in the direction of different phenomena and transitions in the flow topology happening at larger gaps. Finally, the asymptotic values of Ro_{opt}^{-1} obtained in experiments were compared to the speculation of van Gils *et al.* (2012) and the prediction of Brauckmann & Eckhardt (2013*b*). Both of the models were found to deviate from experimental and numerical results.

When looking at the local results, as in Ostilla *et al.* (2013) we can link the optimal transport in the smallest gaps to a balance between Coriolis forces and the inertia terms in the equations of motion. The flattest profiles in the bulk are linked to optimal transport in experiments. With the numerics the extrapolation presented in Ostilla *et al.* (2013) for predicting optimal transport was extended to other radius ratios. It is found to work well for all selected η except for $\eta = 0.5$. At this η, i.e. for the largest gap considered here, the most obvious problem is that the ω profiles strongly feel the effect of curvature difference at the inner and outer cylinders, and a straight-line fit (i.e. $\omega = constant$) to the bulk is not appropriate. There may be additional reasons for this discrepancy, and optimal transport in large gap TC flow requires more investigation. A summary of the results for determining Ro_{opt}^{-1} using both the experimentally measured torque maxima from § 4.2 and the numerical extrapolation from § 5.2 is presented in table 2.

Finally, the boundary layers have been analysed. The outer boundary layer is found to be much thicker than the inner boundary layer when $Ro^{-1} < Ro_{opt}^{-1}$. We attribute this to the appearance of Rayleigh-stable zones in the flow. This prevents the turbulent Taylor vortices from covering the full domain between the cylinders. As the boundary layer size is essentially determined by the wind, if the rolls penetrate the whole domain (which is the case for $Ro^{-1} > Ro_{opt}^{-1}$), the two boundary layers are approximately of the same size. If the rolls do not penetrate the full domain, the outer boundary layer will be much larger than the inner boundary layer, in accordance with the smaller initial slope of $\omega(r)$ at the cylinder walls.

In this work, simulations and experiments have been performed on a range of radius ratios between $0.5 \leqslant \eta \leqslant 0.909$. Insights for the small gaps seem to be consistent with what was discussed in Ostilla *et al.* (2013). However, for $\eta = 0.5$ the phenomenon of optimal transport appears to be quite different. Therefore, our ambition is to extend the DNS towards values of η smaller than 0.5 to improve the understanding of that regime.

Acknowledgements

We would like to thank H. Brauckmann, B. Eckhardt, S. Merbold, M. Salewski, E. P. van der Poel and R. C. A. van der Veen for various stimulating discussions

over the years, and G. W. Bruggert, M. Bos and B. Benschop for technical support. We acknowledge that the numerical results of this research have been achieved using the PRACE-2IP project (FP7 RI-283493) resource VIP based in Germany at Garching. We would also like to thank the Dutch Supercomputing Consortium SurfSARA for technical support and computing resources. We would like to thank FOM, the Simon Stevin Prize of the Technology Foundation STW of The Netherlands, COST from the EU and ERC for financial support through an Advanced Grant.

REFERENCES

AHLERS, G. 1974 Low temperature studies of the Rayleigh–Bénard instability and turbulence. *Phys. Rev. Lett.* **33**, 1185–1188.

AHLERS, G., GROSSMANN, S. & LOHSE, D. 2009 Heat transfer and large scale dynamics in turbulent Rayleigh–Bénard convection. *Rev. Mod. Phys.* **81**, 503–537.

ANDERECK, C. D., LIU, S. S. & SWINNEY, H. L. 1986 Flow regimes in a circular Couette system with independently rotating cylinders. *J. Fluid Mech.* **164**, 155–183.

BEHRINGER, R. P. 1985 Rayleigh–Bénard convection and turbulence in liquid–helium. *Rev. Mod. Phys.* **57**, 657–687.

BENJAMIN, T. B. 1978 Bifurcation phenomena in steady flows of a viscous liquid. *Proc. R. Soc. Lond.* A **359**, 1–43.

BODENSCHATZ, E., PESCH, W. & AHLERS, G. 2000 Recent developments in Rayleigh–Bénard convection. *Annu. Rev. Fluid Mech.* **32**, 709–778.

BRAUCKMANN, H. & ECKHARDT, B. 2013*a* Direct numerical simulations of local and global torque in Taylor–Couette flow up to Re = 30 000. *J. Fluid Mech.* **718**, 398–427.

BRAUCKMANN, H. & ECKHARDT, B. 2013*b* Intermittent boundary layers and torque maxima in Taylor–Couette flow. *Phys. Rev.* E **87**, 033004.

BUSSE, F. H. 1967 The stability of finite amplitude cellular convection and its relation to an extremum principle. *J. Fluid Mech.* **30**, 625–649.

CHANDRASEKHAR, S. 1981 *Hydrodynamic and Hydromagnetic Stability*. Dover.

COUETTE, M. 1890 *Études sur le Frottement des Liquides*. Gauthier-Villars et Fils.

COUGHLIN, K. & MARCUS, P. S. 1996 Turbulent bursts in Couette–Taylor flow. *Phys. Rev. Lett.* **77** (11), 2214–2217.

CROSS, M. C. & HOHENBERG, P. C. 1993 Pattern formation outside of equilibrium. *Rev. Mod. Phys.* **65** (3), 851–1112.

DOMINGUEZ-LERMA, M. A., CANNELL, D. S. & AHLERS, G. 1986 Eckhaus boundary and wavenumber selection in rotating Couette–Taylor flow. *Phys. Rev.* A **34**, 4956–4970.

DONG, S. 2007 Direct numerical simulation of turbulent Taylor–Couette flow. *J. Fluid Mech.* **587**, 373–393.

DONG, S. 2008 Turbulent flow between counter-rotating concentric cylinders: a direct numerical simulation study. *J. Fluid Mech.* **615**, 371–399.

DONNELLY, R. 1991 Taylor–Couette flow: the early days. *Phys. Today* **44** (November), 32–39.

DRAZIN, P. G. & REID, W. H. 1981 *Hydrodynamic Stability*. Cambridge University Press.

ECKHARDT, B., GROSSMANN, S. & LOHSE, D. 2007 Torque scaling in turbulent Taylor–Couette flow between independently rotating cylinders. *J. Fluid Mech.* **581**, 221–250.

ESSER, A. & GROSSMANN, S. 1996 Analytic expression for Taylor–Couette stability boundary. *Phys. Fluids* **8**, 1814–1819.

FASEL, H. & BOOZ, O. 1984 Numerical investigation of supercritical Taylor-vortex flow for a wide gap. *J. Fluid Mech.* **138**, 21–52.

GEBHARDT, TH. & GROSSMANN, S. 1993 The Taylor–Couette eigenvalue problem with independently rotating cylinders. *Z. Phys.* B **90** (4), 475–490.

VAN GILS, D. P. M., BRUGGERT, G. W., LATHROP, D. P., SUN, C. & LOHSE, D. 2011*a* The Twente Turbulent Taylor–Couette (T^3C) facility: strongly turbulent (multi-phase) flow between independently rotating cylinders. *Rev. Sci. Instrum.* **82**, 025105.

VAN GILS, D. P. M., HUISMAN, S. G., BRUGGERT, G. W., SUN, C. & LOHSE, D. 2011*b* Torque scaling in turbulent Taylor–Couette flow with co- and counter-rotating cylinders. *Phys. Rev. Lett.* **106**, 024502.

VAN GILS, D. P. M., HUISMAN, S. G., GROSSMANN, S., SUN, C. & LOHSE, D. 2012 Optimal Taylor–Couette turbulence. *J. Fluid Mech.* **706**, 118–149.

GROSSMANN, S. & LOHSE, D. 2000 Scaling in thermal convection: a unifying view. *J. Fluid Mech.* **407**, 27–56.

GROSSMANN, S. & LOHSE, D. 2001 Thermal convection for large Prandtl number. *Phys. Rev. Lett.* **86**, 3316–3319.

GROSSMANN, S. & LOHSE, D. 2011 Multiple scaling in the ultimate regime of thermal convection. *Phys. Fluids* **23**, 045108.

GROSSMANN, S. & LOHSE, D. 2012 Logarithmic temperature profiles in the ultimate regime of thermal convection. *Phys. Fluids* **24**, 125103.

HUISMAN, S. G., SCHARNOWSKI, S., CIERPKA, C., KAEHLER, C., LOHSE, D. & SUN, C. 2013 Logarithmic boundary layers in highly turbulent Taylor–Couette flow. *Phys. Rev. Lett.* **110**, 264501.

HUISMAN, S. G., VAN GILS, D. P. M. & SUN, C. 2012*a* Applying laser Doppler anemometry inside a Taylor–Couette geometry – using a ray-tracer to correct for curvature effects. *Eur. J. Mech. (*B*/Fluids)* **36**, 115–119.

HUISMAN, S. G., VAN GILS, D. P. M., GROSSMANN, S., SUN, C. & LOHSE, D. 2012*b* Ultimate turbulent Taylor–Couette flow. *Phys. Rev. Lett.* **108**, 024501.

KADANOFF, L. P. 2001 Turbulent heat flow: structures and scaling. *Phys. Today* **54** (8), 34–39.

LATHROP, D. P., FINEBERG, J. & SWINNEY, H. S. 1992*a* Transition to shear-driven turbulence in Couette–Taylor flow. *Phys. Rev.* A **46**, 6390–6405.

LATHROP, D. P., FINEBERG, J. & SWINNEY, H. S. 1992*b* Turbulent flow between concentric rotating cylinders at large Reynolds numbers. *Phys. Rev. Lett.* **68**, 1515–1518.

LEWIS, G. S. & SWINNEY, H. L. 1999 Velocity structure functions, scaling, and transitions in high-Reynolds-number Couette–Taylor flow. *Phys. Rev.* E **59**, 5457–5467.

LOHSE, D. & XIA, K.-Q. 2010 Small-scale properties of turbulent Rayleigh–Bénard convection. *Annu. Rev. Fluid Mech.* **42**, 335–364.

LORENZ, E. N. 1963 Deterministic nonperiodic flow. *J. Atmos. Sci.* **20**, 130–141.

MALLOCK, A. 1896 Experiments on fluid viscosity. *Phil. Trans. R. Soc. Lond.* A **187**, 41–56.

MERBOLD, S., BRAUCKMANN, H. & EGBERS, C. 2013 Torque measurements and numerical determination in differentially rotating wide gap Taylor–Couette flow. *Phys. Rev.* E **87**, 023014.

OSTILLA, R., STEVENS, R. J. A. M., GROSSMANN, S., VERZICCO, R. & LOHSE, D. 2013 Optimal Taylor–Couette flow: direct numerical simulations. *J. Fluid Mech.* **719**, 14–46.

OSTILLA-MÓNICO, R., VAN DER POEL, E. P., VERZICCO, R., GROSSMANN, S. & LOHSE, D. 2014 Boundary layer dynamics at the transition between the classical and the ultimate regime of Taylor–Couette flow. *Phys. Fluids* **26**, 015114.

PAOLETTI, M. S. & LATHROP, D. P. 2011 Angular momentum transport in turbulent flow between independently rotating cylinders. *Phys. Rev. Lett.* **106**, 024501.

PFISTER, G. & REHBERG, I. 1981 Space dependent order parameter in circular Couette flow transitions. *Phys. Lett.* **83**, 19–22.

PFISTER, G., SCHMIDT, H., CLIFFE, K. A. & MULLIN, T. 1988 Bifurcation phenomena in Taylor–Couette flow in a very short annulus. *J. Fluid Mech.* **191**, 1–18.

PIRRO, D. & QUADRIO, M. 2008 Direct numerical simulation of turbulent Taylor–Couette flow. *Eur. J. Mech. (*B*/Fluids)* **27**, 552–566.

SIGGIA, E. D. 1994 High Rayleigh number convection. *Annu. Rev. Fluid Mech.* **26**, 137–168.

SMITH, G. P. & TOWNSEND, A. A. 1982 Turbulent Couette flow between concentric cylinders at large Taylor numbers. *J. Fluid Mech.* **123**, 187–217.

STEVENS, R. J. A. M., LOHSE, D. & VERZICCO, R. 2011 Prandtl and Rayleigh number dependence of heat transport in high Rayleigh number thermal convection. *J. Fluid Mech.* **688**, 31–43.

STEVENS, R. J. A. M., VERZICCO, R. & LOHSE, D. 2010 Radial boundary layer structure and Nusselt number in Rayleigh–Bénard convection. *J. Fluid Mech.* **643**, 495–507.

STROGATZ, S. H. 1994 *Nonlinear Dynamics and Chaos*. Perseus Press.

SWINNEY, H. L. & GOLLUB, J. P. 1981 In *Hydrodynamic Instabilities and the Transition to Turbulence.* Topics in Applied Physics, vol. 45, Springer.

TAYLOR, G. I. 1936 Fluid friction between rotating cylinders. *Proc. R. Soc. Lond.* A **157**, 546–564.

TONG, P., GOLDBURG, W. I., HUANG, J. S. & WITTEN, T. A. 1990 Anisotropy in turbulent drag reduction. *Phys. Rev. Lett.* **65**, 2780–2783.

VERZICCO, R. & ORLANDI, P. 1996 A finite-difference scheme for three-dimensional incompressible flow in cylindrical coordinates. *J. Comput. Phys.* **123**, 402–413.

WENDT, F. 1933 Turbulente Strömungen zwischen zwei rotierenden Zylindern. *Ing.-Arch.* **4**, 577–595.

XIA, K.-Q., LAM, S. & ZHOU, S. Q. 2002 Heat-flux measurement in high-Prandtl-number turbulent Rayleigh–Bénard convection. *Phys. Rev. Lett.* **88**, 064501.